Modeling Spider Webs as Multilinked Structures Using Chebyshev Pseudospectral Collocation

Jennifer N. Green

Thesis submitted to the Faculty of the
Virginia Polytechnic Institute and State University
in partial fulfillment of the requirements for the degree of

Master of Science
in
Mathematics

Mark Embree, Chair
Jeffrey T. Borggaard
Robert C. Rogers

April 27, 2018
Blacksburg, Virginia

Keywords: Spider web, vibrations, Chebyshev collocation

Modeling Spider Webs as Multilinked Structures Using Chebyshev Pseudospectral Collocation

Jennifer N. Green

(ABSTRACT)

Spiders weave intricate webs for catching prey, providing shelter and setting mating rituals; arguably the most notable of these creations is the orb web. In this thesis we model the essential vibrations of orb webs by first considering a spider web as a multilinked structure of elastic strings. We then solve the associated eigenvalue problem using a Chebyshev pseudospectral collocation method to discretize the system. This thesis first examines the vibrations of webs with uniform material properties throughout, then investigates the effects of using biologically realistic material parameters for silks within a single web. Understanding how spiders detect and react to the vibrations produced by their webs is of interest for both biological and engineering applications.

Modeling Spider Webs as Multilinked Structures Using Chebyshev Pseudospectral Collocation

Jennifer N. Green

(GENERAL AUDIENCE ABSTRACT)

Spiders weave intricate webs for catching prey, providing shelter, and setting mating rituals; arguably the most notable of these creations is the orb web. In this thesis we model the essential vibrations of orb webs by first considering a spider web as a multilinked structure of elastic strings. Using numerical methods, we approximate the fundamental frequencies of the web. This thesis first examines the vibrations of webs with uniform material properties throughout, then investigates the effects of biologically realistic parameters of the varying material properties for silks within a single web. Understanding how spiders detect and react to the vibrations produced by their webs is of interest for both biological and engineering applications.

Acknowledgments

I would first like to express my utmost appreciation for Dr. Mark Embree who has taught me many invaluable math and life lessons, including the importance of working in iterations, which makes the daunting task of writing a thesis much more manageable. I would like to thank him for the countless edits and encouragements along the way. I would also like to thank Dr. Brent Opell for his patience in sharing his expertise of spiders and their webs to the novice that I was. Many thanks, as well, go to Dr. Pablo Tarazaga and Dr. Mohammad Albakri for sharing their knowledge of vibrations and, of course, their appreciation of units. I would like to thank Dr. Jeffrey Borggaard and Dr. Robert Rogers for serving on my committee and willingness to answer my many questions. I would like to thank my parents for their continued support and encouragement with all my endeavors whether they be in art, math or dancing. I would like to especially thank my father for his enthusiasm for my current work and experimenting with 3D-printed spider webs. Lastly, I would like to acknowledge my fellow graduate students who persevered alongside me the past two years and especially the last semester.

Contents

List of Figures

List of Tables

Chapter 1

Introduction

Spider webs vary immensely in size and style, from magnificent orb webs to cobwebs in an attic. While the range of usefulness may be overlooked by the human eye, each of these webs serves a very important purpose to the spider that created it. Webs not only serve as a spider's dinner plate, but also as a shelter and the location of mating rituals [5, p. 236]. The vibrations caused by environmental factors, prey, or potential mates all enable the spider to not only discriminate between the different sources, but also help orient the spider to the source of the vibration [9]. Different species of spiders create a variety of webs, which yield endless possibilities for vibrational analysis. Here, we will solely consider orb webs constructed by spiders of the Aranediae family.

1.1 Structure of Orb Webs

Within the Aranediae family, spiders spin orb webs with a wide range of characteristics. Studies have been performed on individual species of spiders within this family, and how vibrations transmit differently through the variations of webs [9, 12, 13]. For example,

using webs constructed by *Nuctenea sclopetaria* in the family Araneidae, Masters studies the transmission of waves within the webs and how these spiders distinguish between wind versus prey induced vibrations [12, 13]. Here, however, we will generalize the most basic structure of orb webs created by different species and look at a specific example of an orb web constructed by a *Argiope trifasciata*. The key structural components of an orb web are the frame threads, radial threads, the catching spiral, a free zone, and a central hub [5]. Figure 1.1 highlights the frame, radial, and catching spiral threads, as they are the main components studied in this thesis. The radial threads attach from frame threads around the edge of the web and meet at the central hub. The catching spiral consists of sticky threads circling the radial webs. This section of the web serves as the location to capture prey [5]. Often a spider will sit motionless in the center of the web (hub) with legs on several radial strands, waiting for a captured prey to send vibrations towards the center [12]. If the spider is not expectantly waiting in the center of the web, it may be hiding in a retreat off to one side of the web, which connects to the web by a signal thread [12].

1.2 Material Properties of Silk in an Orb Web

Not all spider silk is the same. Orb weaver spiders have as many as seven or eight silk glands, which allow them to produce silks with different characteristics [5, 16]. The elasticity, thickness, and stickiness vary for these silks, which proves quite necessary when constructing an orb web. As is expected, there is variation in the properties of silks between species as well. Here we use material properties for the species *Agriope trifasciata* reported by [14, 18].

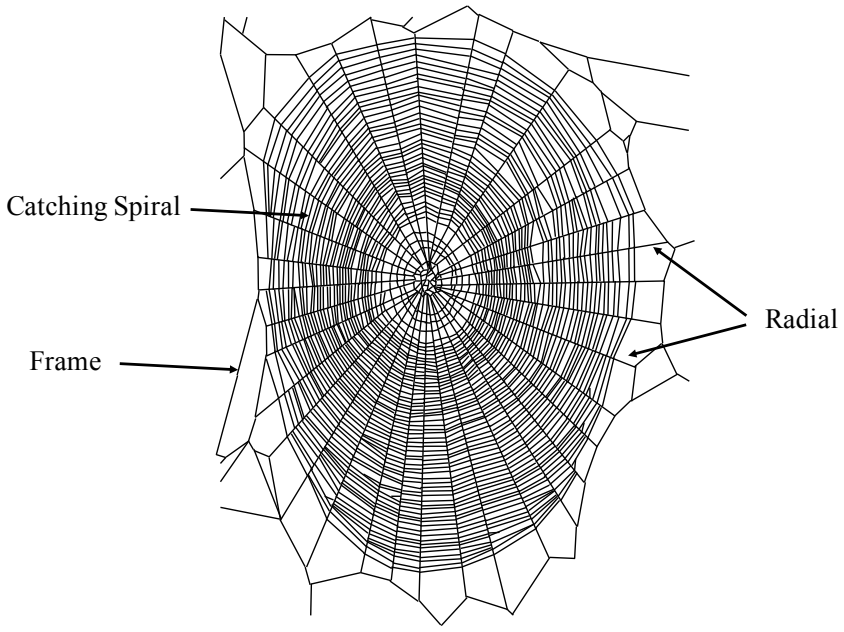

Figure 1.1: Structure of an orb web. Original image taken from [19] and annotated. (This web will be studied further in Chapter 4.)

1.2.1 Frame and Radial Strands

The frame and radial strands provide the main structure for an orb web. The radial components maintain an orb web's structural integrity when it vibrates either from prey impact or environmental factors [3]. These strands are much stronger than those of the catching spiral and provide structural support, shock absorption, and navigational tools for the spider [5]. The stiffness or elasticity of an individual strand of silk is measured by its Young's modulus, reported in Pascals or $\mathrm{kg}/(\mathrm{m} \cdot \mathrm{s}^2)$. Sensenig et al. report the Young's modulus for radial threads as $E = 5.2 \times 10^9$ Pa [18]. Each silk strand consists of two parallel fibers with the diameter of each fiber on average being 3.27 μm [18]. Note that Sensenig et al. only differentiate between "major ampullate" silk used for radial and frame threads and "flag" silk used for the catching spiral [18]. We follow their distinction and group the material properties of frame and radial threads together. Figure 1.2 shows the frame and radial strands of an orb

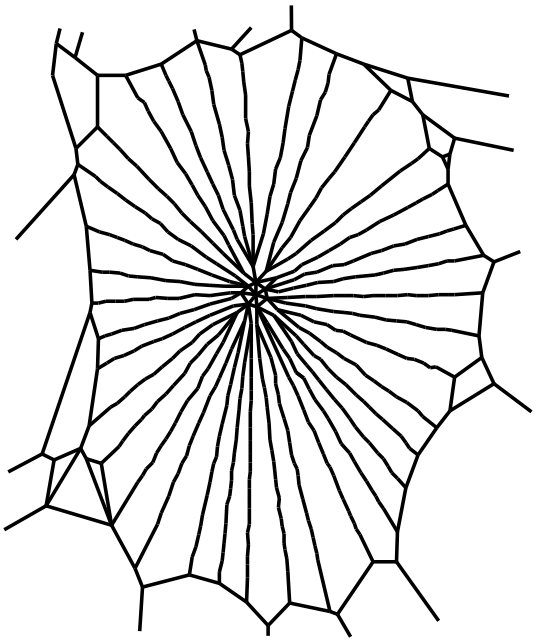

Figure 1.2: Frame and radial strands of an orb web of an *Agriope trifasciata*, traced from the image in Figure 1.1.

web without the catching spiral.

1.2.2 Catching Spiral

The catching spiral provides the actual danger to potential prey. With a Young's modulus of $E = 8 \times 10^6$ Pa [18], these strands are more elastic than the frame and radial threads. The elasticity gives the web the ability to capture struggling prey without suffering excessive damage [5]. Like radial threads, spiral strands also consist of two parallel fibers running alongside each other. However, the catching spiral is additionally coated in an aqueous sheath that coagulates into droplets regularly spaced along the thread [5, 15, 16]. Due to these glue droplets, the capture spiral provides the stickiness most often imagined when we think of spider webs. This structure causes great variation of the cross-sectional area of a

single silk thread over very short lengths. Sensenig et al. report that, on average for an *Agriope trifasciata* spider, there are 16 droplets/mm along a catching spiral strand where the diameter of individual parallel fibers is 2.9 μm each [18]. Using unpublished observations from Dr. Brent Opell [14], at 55% humidity the average length of each droplet is 54 μm and width is 40 μm. All values reported pertain to *Agriope trifasciata*. Note that changes in humidity affect the amount of water in the silk, and thus the elasticity of catching spiral silk [15].

1.2.3 Translation of Web Structure into the Model

Each type of silk has its own properties and purposes within an orb web. For our model, we consider each silk thread as an elastic string. To calculate the vibrations of each string, as well as the web as a whole, requires the knowledge of the density, stiffness, and cross-sectional area of each string. Thus, we calculate the cross-sectional area of the radial, frame, and spiral threads based on rough diameter averages provided in the literature. Also, we assume each strand is a perfect cylinder, with circular cross-section for simplicity of the model. We do not expect our parameters to provide perfectly accurate results for a specific web, but rather to provide a biologically reasonable estimate of silk properties and web vibrations.

Chapter 2

The Model and its Discretization

Our goal is to analyze the vibrations of spider webs, more specifically the eigenmodes of the web, when viewed as a mechanical structure. To study these vibrations, we begin with the wave equation on a single string without damping,

$$u_{tt}(x,t) = c^2 u_{xx}(x,t),$$

for $x \in [0,1]$ and $t \geq 0$, with the homogeneous Dirichlet boundary conditions, $u(0,t) = u(1,t) = 0$. The standard derivation of the wave equation, such as the one provided in [7], gives $c^2 = T/\rho$ where ρ denotes the linear density of the string (kg/m), and T the tension of the string, measured in force (Newtons). The general solution of the corresponding eigenvalue problem $-u_{xx} = \lambda u$ is given by $u(x) = A\sin(\sqrt{\lambda}x) + B\cos(\sqrt{\lambda}x)$. The Dirichlet conditions limit the eigenfunctions to the form $u(x) = \sin(\sqrt{\lambda}x)$ for $\lambda = n^2\pi^2,\ n = 1, 2, \ldots,$ where $\sqrt{\lambda}$ corresponds to a frequency of vibration of the string.

To model spider webs, we will not only consider the movement of a single string, but the movements of many strings linked together as a web. Such a model is motivated by the bio-

logical application, but also provides an appealing example of a partial differential equation on a graph [8]. The following sections describe our problem and how we solve it.

2.1 The Wave Equation

We make several assumptions about the general structure of a spider web. First, we assume the web is anchored with no "free flowing" ends. At these anchored points we impose homogeneous Dirichlet boundary conditions. Second, we require the connections between individual strands to remain intact while the web moves. Not only must they remain attached, but the slopes of the connected strings must match: the web should not form "kinks" at the junctions. We must account for these conditions on each strand of the web. Between its end points, we assume that each strand behaves as a vibrating string, governed by the wave equation in three physical dimensions. As the web vibrates, the nodes where the strands meet can move in three dimensions, while the boundary nodes are fixed. We do not account for damping on the strings in the basic model studied in this thesis.

We begin our analysis by examining the planar vibrations of an elastic string in $\mathbb{R}^2$. (Our model will account for vibrations in $\mathbb{R}^3$ later in the chapter.) The conditions described above lead us to the model of a dynamic network of elastic strings proposed by Lagnese, Leurering, and Schmidt [8, 17] and elucidated by Cox [1]. Their work provides a strong basis for us to build a discretization of a very specific elastic multi-link structure. Appealing to their model, we define the following parameters for strand i of the spider web: length ℓ^i; density ρ^i; stiffness k^i; orientation $\mathbf{v}^i \in \mathbb{R}^3$; and an internal measure of tension σ^i. Here ρ^i is again linear density with units kg/m, k^i is measured in Newtons and σ^i is a constant without units. Let $\mathbf{r}_i(s,t)$ denote the planar displacement of the ith string within the web. Here s varies along the length of the string: $s \in [0, \ell^i]$. Consider the partial differential equation for each

string's planar displacement,

$$\rho^i \mathbf{r}^i_{tt} = \mathbf{P}^i \mathbf{r}^i_{ss}, \tag{2.1}$$

where

$$\mathbf{P}^i = k^i[(\sigma^i - 1)\mathbf{I} + \mathbf{v}^i \mathbf{v}^{i*}] \tag{2.2}$$

and $\mathbf{I}$ is the 2×2 identity matrix (or the 3×3 identity matrix for vibrations in $\mathbb{R}^3$). Here $\sigma^i > 1$ implies a stretched string, while $\sigma^i < 1$ implies a compressed string. $\mathbf{P}^i$ accounts for the tension, stretching, and orientation of the string. For a detailed derivation of this PDE, see [8]. When considering vibrations in $\mathbb{R}^2$, each planar displacement will have two components, which we denote as $\mathbf{r}^{i,x}$ and $\mathbf{r}^{i,y}$. When transitioning to three dimensions, we include $\mathbf{r}^{i,z}$ as well.

To first test our model, we analyze two strings (of length ℓ^1 and ℓ^2) attached together in a straight line, as in Figure 2.1. For this trivial example the dynamics will be exactly those of a single string, and are thus well known and easily verified. Here we have the eigenvalue problem

$$-\mathbf{P}^i \mathbf{r}^i_{ss} = \lambda \rho^i \mathbf{r}^i \tag{2.3}$$

for $i = 1, 2$, with Dirichlet boundary conditions

$$\mathbf{r}^1(0, t) = 0, \tag{2.4}$$

$$\mathbf{r}^2(\ell^2, t) = 0, \tag{2.5}$$

and orientation

$$\mathbf{v}^1 = \mathbf{v}^2 = \begin{bmatrix} 1 \\ 0 \end{bmatrix}. \tag{2.6}$$

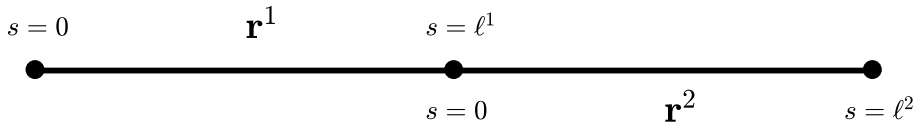

Figure 2.1: The simplest form of the model: two strings attached in the middle, forming a straight line. Note the start of each string at $s = 0$ and the end of each string at $s = \ell^i$. $i = 1, 2$.

Now we need the continuity condition

$$\mathbf{r}^1(\ell^1, t) = \mathbf{r}^2(0, t), \tag{2.7}$$

and we must maintain smoothness at the junction. We state first the slope interface condition derived by Schmidt in both [17] and [8],

$$\mathbf{P}^1\mathbf{r}_s^1(\ell^1, t) - \mathbf{P}^2\mathbf{r}_s^2(0, t) = 0. \tag{2.8}$$

While the conditions preceding this one followed in a straightforward manner, this condition is of special interest. This dynamic boundary condition is obtained during the derivation of the partial differential equation, and is a result of "free" or "natural" boundary conditions, obtained using a calculus of variations argument [8].

2.2 Discretization

To discretize the eigenvalue problem above, we apply the Chebyshev pseudospectral collocation method described by Trefethen [20]. Our approach approximates the displacement of each string using polynomial interpolation at a grid of points spanning $[0, \ell^i]$. We choose

Chebyshev points for our grid, rather than uniformly distributed points; see [20] for more information on why Chebyshev points, which cluster near the boundaries, give better approximation properties than uniform points for polynomial interpolation. Let $\mathcal{P}_n$ denote the set of polynomials of degree n or less. Given $f \in C[0, \ell]$ and $N+1$ distinct points $\{s_j\}_{j=0}^{N} \subset [0, \ell^i]$, we determine $p_n \in \mathcal{P}_n$ such that $p_n(s_j) = f(s_j)$ for all $j = 0, \ldots, N$. Our grid will consist of the Chebyshev points

$$s_j = \frac{\ell}{2}\left(1 + \cos\left(\frac{j\pi}{N}\right)\right), \quad j = 0, \ldots, N. \tag{2.9}$$

2.2.1 Chebyshev Differentiation Matrix

The Chebyshev points we have chosen cluster toward the ends of each strand, rather than providing uniform distances between each point. This property makes derivative approximation more intricate than for lower order interpolation on a uniform grid. We will first show the case where $N = 1$ to demonstrate the construction and purpose of our differentiation matrix. Let $N = 1$, and s_0 and s_1 be the Chebyshev points chosen based on our interval. Define $v_0 = v(s_0) = c_0 + c_1 s_0$ and $v_1 = v(s_1) = c_0 + c_1 s_1$, where c_0 and c_1 are constants. From here the goal is to find c_0 and c_1 from v_0 and v_1. First we write our problem as a linear system of equations:

$$\begin{bmatrix} 1 & s_0 \\ 1 & s_1 \end{bmatrix} \begin{bmatrix} c_0 \\ c_1 \end{bmatrix} = \begin{bmatrix} v_0 \\ v_1 \end{bmatrix}.$$

Let $\mathbf{S} = \begin{bmatrix} 1 & s_0 \\ 1 & s_1 \end{bmatrix}$, and $\mathbf{v} = \begin{bmatrix} v_0 \\ v_1 \end{bmatrix}$, so that

$$\begin{bmatrix} c_0 \\ c_1 \end{bmatrix} = \mathbf{S}^{-1}\mathbf{v}.$$

Now the derivative of v gives $v'(s_0) = v'(s_1) = c_1$, so

$$\mathbf{v}' = \begin{bmatrix} v'(s_0) \\ v'(s_1) \end{bmatrix} = \begin{bmatrix} c_1 \\ c_1 \end{bmatrix}.$$

Our goal is to find $\mathbf{D}$ such that $\mathbf{Dv} = \mathbf{v}'$. Thus we can write

$$\begin{bmatrix} 0 & 1 \\ 0 & 1 \end{bmatrix} \mathbf{S}^{-1} \begin{bmatrix} v_0 \\ v_1 \end{bmatrix} = \begin{bmatrix} 0 & 1 \\ 0 & 1 \end{bmatrix} \begin{bmatrix} c_0 \\ c_1 \end{bmatrix} = \begin{bmatrix} c_1 \\ c_1 \end{bmatrix} = \mathbf{v}'.$$

Define $\mathbf{D} = \begin{bmatrix} 0 & 1 \\ 0 & 1 \end{bmatrix} \mathbf{S}^{-1}$, so that $\mathbf{Dv} = \mathbf{v}'$. This concept can be applied for any $N \geq 1$. From here we will define $\mathbf{D}_N$ as the $(N+1) \times (N+1)$ Chebyshev differentiation matrix for a polynomial $v \in \mathcal{P}_N$. The elements of $\mathbf{D}_N$ can be defined by formulas provided in [20]. Using these formulas and the very specific structure they encode, Trefethen constructs MATLAB code to construct this differentiation matrix for Chebyshev points on the interval $s \in [-1, 1]$. We altered the code to create $\mathbf{D}_N$ for a string with $s \in [0, \ell]$. We follow Trefethen's convention, with the Chebyshev formula (2.9) labeling the points from right to left:

$$s_0 = \ell, \qquad s_N = 0.$$

We will use this altered version to create different $\mathbf{D}_N$, sized for strands of different lengths ℓ^i within the spider web.

The beauty of $\mathbf{D}_N$ is that its square will provide the second derivative of $\mathbf{v}$:

$$\mathbf{D}_N\mathbf{v} = \mathbf{v}' \quad \text{and} \quad (\mathbf{D}_N)^2\mathbf{v} = \mathbf{v}''.$$

This groundwork allows us to discretize the eigenvalue problem. We can now approximate the continuous eigenvalue problem, $\mathbf{P}^i\mathbf{r}^i_{ss} = \lambda\rho\mathbf{r}^i$ over $s \in [0, \ell]$ with the discrete problem.

2.2.2 Solving the Eigenvalue Problem

To discretize equation (2.3), we first apply the discretization to a simpler problem of the same vein.

Example 1

Consider the partial differential equation $-u_{ss}(s) = \lambda u(s)$ on $s \in [0, 1]$ sampled at $N + 1$ Chebyshev points, $s_0, \ldots, s_N$, with boundary conditions $u_0 = u(1) = u(s_0) = 0$ and $u_N = u(0) = u(s_N) = 0$. (Note that for the ith string, $s_0 = \ell^i$ and $s_N = 0$.) Based on the previous section we know $((\mathbf{D}_N)^2\mathbf{u})_j = \mathbf{u}_{ss}(s_j)$. Then we write the eigenvalue problem $-(\mathbf{D}_N)^2\mathbf{u} = \lambda\mathbf{u}$, where

$$\mathbf{u} = \begin{bmatrix} u_0 \\ \vdots \\ u_N \end{bmatrix}.$$

The boundary conditions further give $u(s_0) = u(s_N) = 0$. To implement these conditions in our discretization, we zero out u_0 and u_N on the right hand side of the equation. To account

for these conditions on the left hand side, we set up the system of equations

$$\left[\begin{array}{c|c|c} 1 & 0 \quad \cdots \quad 0 & 0 \\ \hline & -(\mathbf{D}_N)^2(2:N,:) & \\ \hline 0 & 0 \quad \cdots \quad 0 & 1 \end{array}\right] \begin{bmatrix} u_0 \\ u_1 \\ \vdots \\ u_{N-1} \\ u_N \end{bmatrix} = \lambda \left[\begin{array}{c} 0 \\ \hline u_1 \\ \vdots \\ u_{N-1} \\ \hline 0 \end{array}\right].$$

Replacing the first row of the discretization matrix with zeros except for the entry corresponding to u_0 gives the first equation of the system as $u_0 = \lambda \cdot 0 = 0$. Similarly, we disregard the last row of $(\mathbf{D}_N)^2$ and replace it with the condition for $u_N = 0$. Now the discretization implements the boundary conditions, as well as the partial differential equation. Since including the boundary conditions removes the first and last rows of $(\mathbf{D}_N)^2$, we are left with rows 2 through N. Thus $-(\mathbf{D}_N)^2(2:N,:)$ has dimensions $(N-1) \times (N+1)$ as expected. Now to solve for $\mathbf{u}$ we introduce the generalized eigenvalue problem:

$$\left[\begin{array}{c|c|c} 1 & 0 \quad \cdots \quad 0 & 0 \\ \hline & -(\mathbf{D}_N)^2(2:N,:) & \\ \hline 0 & 0 \quad \cdots \quad 0 & 1 \end{array}\right] \begin{bmatrix} u_0 \\ u_1 \\ \vdots \\ u_{N-1} \\ u_N \end{bmatrix} = \lambda \left[\begin{array}{c|c|c} 0 & 0 \quad \cdots \quad 0 & 0 \\ \hline 0 & & 0 \\ \vdots & \mathbf{I}_{N-1} & \vdots \\ 0 & & 0 \\ \hline 0 & 0 \quad \cdots \quad 0 & 0 \end{array}\right] \begin{bmatrix} u_0 \\ u_1 \\ \vdots \\ u_{N-1} \\ u_N \end{bmatrix}.$$

Here, the addition of the right-hand matrix achieves the exact same effect of "zeroing" out the first and last entries of $\mathbf{u}$ without altering the middle entries. Note that the values of λ that satisfy this structure are simply the eigenvalues of the generalized eigenvalue problem $\mathbf{Au} = \lambda\mathbf{Bu}$, where $\mathbf{u}$ is the eigenvector. Finding possible λ and corresponding $\mathbf{u}$ here requires little more than calling the function `eig(A, B)` in MATLAB. For Dirichlet boundary conditions,

the generalized eigenvalue framework may seem overly elaborate. However, more complicated boundary conditions implemented below illustrate the utility of this approach.

Example 2

If rather than $u(1) = 0$ we have the condition $u'(1) = 0$, we can solve a similar system. Recall that $(\mathbf{D}_N\mathbf{u})_j = \mathbf{u}'(s_j)$. The condition $u'(1) = 0$ implies that $(\mathbf{D}_N\mathbf{u})_1 = 0$. Thus we can take the corresponding row from $\mathbf{D}_N$ to implement this condition:

$$\left[\begin{array}{c} \mathbf{D}_N(1,:) \\ \hline \\ -\mathbf{D}_N^2(2:N,:) \\ \\ \hline 0 \quad 0 \quad \cdots \quad 0 \quad 1 \end{array}\right] \begin{bmatrix} u_0 \\ u_1 \\ \vdots \\ u_{N-1} \\ u_N \end{bmatrix} = \lambda \left[\begin{array}{c|c|c} 0 & 0 \cdots 0 & 0 \\ \hline 0 & & 0 \\ \vdots & \mathbf{I}_{N-1} & \vdots \\ 0 & & 0 \\ \hline 0 & 0 \cdots 0 & 0 \end{array}\right] \left[\begin{array}{c} 0 \\ \hline u_1 \\ \vdots \\ u_{N-1} \\ \hline 0 \end{array}\right],$$

where $\mathbf{D}_N(1,:)$ represents the first row and all columns of $\mathbf{D}_N$, and $(\mathbf{D}_N)^2(2:N,:)$ represents the second through Nth rows of $(\mathbf{D}_N)^2$. As before, we can solve the new $(N+1)\times(N+1)$ generalized eigenvalue problem for $\mathbf{u} = [u_0, \ldots, u_N]^T$.

2.3 Discretization of the Two-string Example

We illustrate the discretization process with the simple example of two strings connected together, as studied earlier. Note that equation (2.3) can be written as

$$-\mathbf{P}^i \begin{bmatrix} \mathbf{r}_{ss}^{i,x} \\ \mathbf{r}_{ss}^{i,y} \end{bmatrix} = \lambda^i \rho^i \begin{bmatrix} \mathbf{r}^{i,x} \\ \mathbf{r}^{i,y} \end{bmatrix},$$

where $\mathbf{P}^i$ is a 2×2 matrix in the two-string example. Discretize the eigenvalue equation (2.3) as outlined above, giving an equation in 2(N+1) variables $\mathbf{r}^i$ for each $i = 1, 2$:

$$-\mathbf{P}^i_{\otimes} \begin{bmatrix} (\mathbf{D}^{(i)})^2 \mathbf{r}^{i,x} \\ (\mathbf{D}^{(i)})^2 \mathbf{r}^{i,y} \end{bmatrix} = \lambda^i \rho^i \begin{bmatrix} \mathbf{r}^{i,x} \\ \mathbf{r}^{i,y} \end{bmatrix}. \tag{2.10}$$

Here $\mathbf{D}^{(i)}$ denotes the differentiation matrix $\mathbf{D}_N$ for string i. Note for ease of notation, we no longer denote $\mathbf{D}$ with an N, as N stays the same throughout each example. Both $\mathbf{r}^{i,x}$ and $\mathbf{r}^{i,y}$ are column vectors of length $(N+1)$. We define $\mathbf{P}^i_{\otimes}$ as the Kronecker product of $\mathbf{P}^i$ with the $N+1$ dimensional identity $(\mathbf{P}^i \otimes \mathbf{I})$, which has dimension $2(N+1)$:

$$\mathbf{P}^i_{\otimes} = \begin{bmatrix} \mathbf{P}^i_{11}\mathbf{I} & \mathbf{P}^i_{12}\mathbf{I} \\ \mathbf{P}^i_{21}\mathbf{I} & \mathbf{P}^i_{22}\mathbf{I} \end{bmatrix}.$$

Remembering the boundary, continuity, and slope conditions in equations (2.4) – (2.8), we can apply the same concept of replacing rows of equation (2.10) with the boundary and slope conditions. There is an important difference between our model and one dimensional Examples 1 and 2 above, where each boundary condition resulted in zeroing out u_0 or u_N. The higher complexity of the continuity and slope conditions requires a slight alteration to the described discretization. Here the implementation of the generalized eigenvalue problem becomes quite useful, as we can account for the slope and continuity conditions required to verify consistent junctions of the spider web easily. In the structure

$$\mathbf{A}\mathbf{r} = \lambda \mathbf{B}\mathbf{r}, \tag{2.11}$$

let $\mathbf{A}$ reference the combination of the $\mathbf{D}_N$ matrix and the boundary conditions, and $\mathbf{r}$ be the vector of displacements for all strings in the network. Then the entries of $\mathbf{B}$ are chosen so

that each row either enforces the eigenvalue equation, or completes a boundary, continuity, or slope condition. Since $\mathbf{B}$ allows for any $\mathbf{r}^i$ value to be set in any row of the system, the row placement of the conditions is not important. Using the generalized eigenvalue structure, for each equation in the system we simply set the corresponding row of $\mathbf{B}$ to satisfy the desired equation. Note that each string has x, y, and z components. For simplicity we will only show x and y components in the example below. (The extension to 3D is straightforward enough and follows readily.) For Table 2.1, we employ shorter notation for readability. Let $(\mathbf{D}^{(i)})_{j:k}$ represent rows j through k of the Chebyshev differentiation matrix for the ith string. Likewise, $(\mathbf{D}^{(i)})^2_{j:k}$ represents rows j through k of the square of the ith differentiation matrix. (The matrix is squared prior to taking the rows.) Table 2.2 describes how each row of our discretization in Table 2.1 pertains to the boundary value problem. For convenience, we will denote the displacement of the x component of the ith string at $s = \ell^i$ by $\overline{\mathbf{r}^{i,x}}(t) \in \mathbb{R}$, at $s = 0$ by $\underline{\mathbf{r}^{i,x}}(t) \in \mathbb{R}$, and on the interior grid points by $\mathbf{r}^{i,x}(t) \in \mathbb{R}^{N-1}$. Analogous notation applies for the y components. Note that the slope and continuity conditions do not include information about λ. Rearranging equation (2.7) to be

$$\mathbf{r}^{1,x}(\ell^1, t) - \mathbf{r}^{2,x}(0, t) = 0,$$

(with analogous equation for the y components), so we zero out the corresponding row of $\mathbf{B}$. To account for equation (2.8), implement two rows of the system of equations as

$$\mathbf{P}^1_{\otimes} \begin{bmatrix} (\mathbf{D}^{(1)})_1 \mathbf{r}^{1,x} \\ (\mathbf{D}^{(1)})_1 \mathbf{r}^{1,y} \end{bmatrix} - \mathbf{P}^2_{\otimes} \begin{bmatrix} (\mathbf{D}^{(2)})_{N+1} \mathbf{r}^{2,x} \\ (\mathbf{D}^{(2)})_{N+1} \mathbf{r}^{2,y} \end{bmatrix} = 0,$$

where the corresponding rows of $\mathbf{B}$ are rows of all zeros. Where $(\mathbf{D}^{(1)})_1$ corresponds to the first row of $\mathbf{D}^{(1)}$ and $(\mathbf{D}^{(2)})_{N+1}$ corresponds to the last row of $\mathbf{D}^{(2)}$. We now implement the generalized eigenvalue problem for the two-string example.

Table 2.1: The generalized eigenvalue problem $\mathbf{Ar} = \lambda\mathbf{Br}$ associated with the simple two-string model.

$$
\begin{array}{c}
\\
(1)\\
(2)\\
(3)\\
(4)\\
(5)\\
(6)\\
(7)\\
(8)\\
(9)
\end{array}
\left[\begin{array}{ccc|ccc|ccc|ccc}
0 & \mathbf{0} & 1 & 0 & \mathbf{0} & 0 & 0 & \mathbf{0} & 0 & 0 & \mathbf{0} & 0 \\
\hline
0 & \mathbf{0} & 0 & 0 & \mathbf{0} & 1 & 0 & \mathbf{0} & 0 & 0 & \mathbf{0} & 0 \\
\hline
\multicolumn{6}{c|}{-\mathbf{P}^1_{\otimes}\begin{bmatrix}(\mathbf{D}^{(1)})^2_{2:N}\\(\mathbf{D}^{(1)})^2_{2:N}\end{bmatrix}} & \mathbf{0} & \mathbf{0} & \mathbf{0} & \mathbf{0} & \mathbf{0} & \mathbf{0} \\
\multicolumn{6}{c|}{} & \mathbf{0} & \mathbf{0} & \mathbf{0} & \mathbf{0} & \mathbf{0} & \mathbf{0} \\
\hline
1 & \mathbf{0} & 0 & 0 & \mathbf{0} & 0 & 0 & \mathbf{0} & -1 & 0 & \mathbf{0} & 0 \\
\hline
0 & \mathbf{0} & 0 & 1 & \mathbf{0} & 0 & 0 & \mathbf{0} & 0 & 0 & \mathbf{0} & -1 \\
\hline
\multicolumn{3}{c|}{\mathbf{P}^1_{\otimes}\begin{bmatrix}(\mathbf{D}^{(1)})_1\\(\mathbf{D}^{(1)})_1\end{bmatrix}} & \multicolumn{3}{c|}{-\mathbf{P}^2_{\otimes}\begin{bmatrix}(\mathbf{D}^{(2)})_{N+1}\\(\mathbf{D}^{(2)})_{N+1}\end{bmatrix}} \\
\hline
0 & \mathbf{0} & 0 & 0 & \mathbf{0} & 0 & \multicolumn{3}{c|}{\multirow{2}{*}{$-\mathbf{P}^2_{\otimes}\begin{bmatrix}(\mathbf{D}^{(2)})^2_{2:N}\\(\mathbf{D}^{(2)})^2_{2:N}\end{bmatrix}$}} \\
0 & \mathbf{0} & 0 & 0 & \mathbf{0} & 0 & \multicolumn{3}{c|}{} \\
\hline
0 & \mathbf{0} & 0 & 0 & \mathbf{0} & 0 & 1 & \mathbf{0} & 0 & 0 & \mathbf{0} & 0 \\
\hline
0 & \mathbf{0} & 0 & 0 & \mathbf{0} & 0 & 0 & \mathbf{0} & 0 & 1 & \mathbf{0} & 0
\end{array}\right]
\left[\begin{array}{c}
\overline{\mathbf{r}^{1,x}}\\
\mathbf{r}^{1,x}\\
\underline{\mathbf{r}^{1,x}}\\
\hline
\overline{\mathbf{r}^{1,y}}\\
\mathbf{r}^{1,y}\\
\underline{\mathbf{r}^{1,y}}\\
\hline
\overline{\mathbf{r}^{2,x}}\\
\mathbf{r}^{2,x}\\
\underline{\mathbf{r}^{2,x}}\\
\hline
\overline{\mathbf{r}^{2,y}}\\
\mathbf{r}^{2,y}\\
\underline{\mathbf{r}^{2,y}}
\end{array}\right]
= \lambda
\left[\begin{array}{ccc|ccc|ccc|ccc}
0 & \mathbf{0} & 0 & 0 & \mathbf{0} & 0 & 0 & \mathbf{0} & 0 & 0 & \mathbf{0} & 0 \\
\hline
0 & \mathbf{0} & 0 & 0 & \mathbf{0} & 0 & 0 & \mathbf{0} & 0 & 0 & \mathbf{0} & 0 \\
\hline
\mathbf{0} & \mathbf{I} & \mathbf{0} & \mathbf{0} & \mathbf{0} & \mathbf{0} & \mathbf{0} & \mathbf{0} & \mathbf{0} & \mathbf{0} & \mathbf{0} & \mathbf{0} \\
\hline
\mathbf{0} & \mathbf{0} & \mathbf{0} & \mathbf{0} & \mathbf{I} & \mathbf{0} & \mathbf{0} & \mathbf{0} & \mathbf{0} & \mathbf{0} & \mathbf{0} & \mathbf{0} \\
\hline
0 & \mathbf{0} & 0 & 0 & \mathbf{0} & 0 & 0 & \mathbf{0} & 0 & 0 & \mathbf{0} & 0 \\
\hline
0 & \mathbf{0} & 0 & 0 & \mathbf{0} & 0 & 0 & \mathbf{0} & 0 & 0 & \mathbf{0} & 0 \\
\hline
0 & \mathbf{0} & 0 & 0 & \mathbf{0} & 0 & 0 & \mathbf{0} & 0 & 0 & \mathbf{0} & 0 \\
\hline
0 & \mathbf{0} & 0 & 0 & \mathbf{0} & 0 & 0 & \mathbf{0} & 0 & 0 & \mathbf{0} & 0 \\
\hline
\mathbf{0} & \mathbf{0} & \mathbf{0} & \mathbf{0} & \mathbf{0} & \mathbf{0} & \mathbf{0} & \mathbf{I} & \mathbf{0} & \mathbf{0} & \mathbf{0} & \mathbf{0} \\
\hline
\mathbf{0} & \mathbf{0} & \mathbf{0} & \mathbf{0} & \mathbf{0} & \mathbf{0} & \mathbf{0} & \mathbf{0} & \mathbf{0} & \mathbf{0} & \mathbf{I} & \mathbf{0} \\
\hline
0 & \mathbf{0} & 0 & 0 & \mathbf{0} & 0 & 0 & \mathbf{0} & 0 & 0 & \mathbf{0} & 0 \\
\hline
0 & \mathbf{0} & 0 & 0 & \mathbf{0} & 0 & 0 & \mathbf{0} & 0 & 0 & \mathbf{0} & 0
\end{array}\right]
\left[\begin{array}{c}
\overline{\mathbf{r}^{1,x}}\\
\mathbf{r}^{1,x}\\
\underline{\mathbf{r}^{1,x}}\\
\hline
\overline{\mathbf{r}^{1,y}}\\
\mathbf{r}^{1,y}\\
\underline{\mathbf{r}^{1,y}}\\
\hline
\overline{\mathbf{r}^{2,x}}\\
\mathbf{r}^{2,x}\\
\underline{\mathbf{r}^{2,x}}\\
\hline
\overline{\mathbf{r}^{2,y}}\\
\mathbf{r}^{2,y}\\
\underline{\mathbf{r}^{2,y}}
\end{array}\right]
$$

Table 2.2: Description of labeled rows of **A** in equation (2.1), along with the number of individual rows accounted for by each label. *(For simplicity we assume $\rho = 1$ in the two string example.)

	Condition	# Rows		Condition	# Rows
(1)	$\underline{\mathbf{r}^{1,x}} = 0$	1	(6)	$\mathbf{P}^1\mathbf{r}_s^1 = \mathbf{P}^2\mathbf{r}_s^2$	2
(2)	$\underline{\mathbf{r}^{1,y}} = 0$	1			
(3)*	$\mathbf{P}^1\mathbf{r}_{ss}^1 = \lambda\rho\mathbf{r}^1$	$2(N-1)$	(7)*	$\mathbf{P}^2\mathbf{r}_{ss}^2 = \lambda\rho\mathbf{r}^2$	$2(N-1)$
(4)	$\overline{\mathbf{r}^{1,x}} = \underline{\mathbf{r}^{2,x}}$	1	(8)	$\overline{\mathbf{r}^{2,x}} = 0$	1
(5)	$\overline{\mathbf{r}^{1,y}} = \underline{\mathbf{r}^{2,y}}$	1	(9)	$\overline{\mathbf{r}^{2,y}} = 0$	1

In Table 2.2, note that the first and third columns for the separate strings in **A** and **B** correspond to the last and first point on individual strings, while the middle bold column corresponds to all of the interior points of that string. This format is chosen since the ends of the string are treated differently than the interior, because the boundary and slope conditions strictly apply to the ends. From here, we solve the generalized eigenvalue problem to find eigenvalues for our system. Using these values and the corresponding eigenvectors, we can then visualize the movements of each eigenmode for the two string example. As expected, these computed eigenvalues are the same as those of a single string. Since we are interested in a network of strings, we will now use the process described above to create larger and more exciting networks.

2.4 The Tritare

After implementing the two-string example, the next step adds a third string; the resulting arrangement models a "tritare," a guitar-like instrument with a forked string shown in Figure 2.2. In the tritare each guitar string is replaced by a network of three strings connected

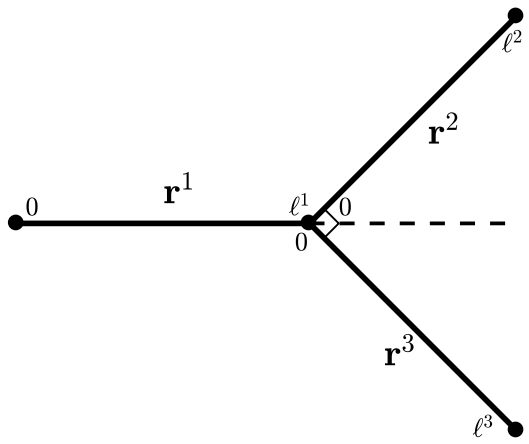

Figure 2.2: The 3-string tritare. Here each leg is the same length, which differs slightly from the original structure in [6]. Each string $\mathbf{r}^i$ is labeled from the start of the string, $s = 0$, to the end, $s = \ell^i$, for $i = 1, 2, 3$.

in a 'Y' shape. Gaudet et al. [6] created this instrument to study the vibrations and sounds this different string structure would give. We use this structure to compare the eigenvalues obtained from the current model with those obtained analytically, thus verifying the validity of the numerical discretization.

2.4.1 Discretization

We apply the discretization described above to the tritare to compare the computed eigenvalues of this simple web (or multi-link structure) with the exact eigenvalues of the system. Here the wave equation stays the same, but now $i = 1, 2, 3$. The strings have orientations

$$\mathbf{v}^1 = \begin{bmatrix} 1 \\ 0 \end{bmatrix}, \quad \mathbf{v}^2 = \begin{bmatrix} \frac{1}{\sqrt{2}} \\ \frac{1}{\sqrt{2}} \end{bmatrix}, \quad \mathbf{v}^3 = \begin{bmatrix} \frac{1}{\sqrt{2}} \\ -\frac{1}{\sqrt{2}} \end{bmatrix}.$$

Here we set $\rho^i = 1$ and $\sigma^i = 2$ for $i = 1, 2, 3$. We define any node that only has one edge connection as a boundary node and nodes with multiple connections as inner nodes. We have boundary conditions $\mathbf{r}^1(0,t) = 0$, $\mathbf{r}^2(\ell^2,t) = 0$, and $\mathbf{r}^3(\ell^3,t) = 0$. We must address the connection of the three edges. At each junction between edges, we apply the continuity condition and the slope condition. The tritare requires the two continuity conditions $\mathbf{r}^1(\ell^1,t) = \mathbf{r}^2(0,t)$ and $\mathbf{r}^1(\ell^1,t) = \mathbf{r}^3(0,t)$. (Adding the third continuity condition $\mathbf{r}^2(\ell^1,t) = \mathbf{r}^3(0,t)$ would provide no new information and thus is redundant.) The slope interface condition for the tritare is

$$\mathbf{P}^1\mathbf{r}_s^1(\ell^1,t) = \mathbf{P}^2\mathbf{r}_s^2(0,t) + \mathbf{P}^3\mathbf{r}_s^3(0,t).$$

For each junction, the sum of the slopes of the strings that end at the connection must equal the sum of the slopes of the strings that begin at the connection. This condition is a direct extension of the condition described by [8]. The discretization for the tritare then leads us to solving the generalized eigenvalue problem similar to that of equation (2.1). The tritare differs from the two-string example in several ways. First, the third string contributes additional rows and columns to the discretization matrices, $\mathbf{A}$ and $\mathbf{B}$. Here $\mathbf{A}$ and $\mathbf{B}$ will have dimension $6(N+1)\times 6(N+1)$ for the two dimensional case and $9(N+1)\times 9(N+1)$ when considering displacements in $\mathbb{R}^3$. Second, the changes in the slope and continuity conditions will alter the corresponding rows of $\mathbf{A}$ and $\mathbf{B}$. To study the convergence of the algorithm, we solve the system for several values of N.

2.4.2 Comparison to Exact Solutions

In the case of the tritare, the PDE eigenvalue problem can be reduced to the roots of four transcendental equations [4]. It can be shown that the eigenvalues of the system fall into

four categories:

$$\text{A: roots of } \sin(\lambda) = 0; \tag{2.12}$$

$$\text{B: roots of } \sin\left(\frac{\lambda}{\sqrt{2}}\right) = 0; \tag{2.13}$$

$$\text{C: roots of } \tan(\lambda) = -\sqrt{2}\tan\left(\frac{\lambda}{\sqrt{2}}\right); \tag{2.14}$$

$$\text{D: roots of } \tan(\lambda) = -\frac{1}{2\sqrt{2}}\tan\left(\frac{\lambda}{\sqrt{2}}\right). \tag{2.15}$$

The eigenvalues were computed using root solving algorithms in Mathematica to very high precision, with results shown in Table 2.3. (Gaudet et al. [6] also compute the exact eigenvalues for a tritare with slightly different properties that align, as we would expect, with those shown in Table 2.3, and those computed by the discretization.) In Table 2.4 we compare the exact eigenvalues calculated with those found using the Chebyshev discretization for $N = 8, 16, 32$, and 64. Note that the accuracy increases with the number of Chebyshev points until $N = 16$ or $N = 32$. For lower eigenvalues $(\lambda_1, \ldots, \lambda_6)$ when $N = 32$ and $N = 64$ we either do not gain additional digits of accuracy or even lose a digit of accuracy. (This loss of accuracy is likely due to the increase of $\|\mathbf{A}\|$ as N increases.) For the remaining eigenvalues displayed in Table 2.4, $N = 32$ provides the highest level of accuracy. In either case, these observations show the accuracy that can be achieved through the discretization with relatively few Chebyshev points. To further demonstrate the convergence of our model and the previous observations, Figure 2.3 compares the computed eigenvalues to the exact ones for several values of N. The loss of accuracy for $N > 16$ for smaller eigenvalues is shown on the left; the loss of accuracy for $N > 32$ for larger eigenvalues is shown on the right.

Table 2.3: The exact eigenvalues of the 2D tritare.

i	*type*	*eigenvalue*
1	C	1.78993037359553312790910971176275339411025382465 46
2	D	1.99658732056910586526458512505387816062191235986 26
3	A	3.14159265358979323846264338327950288419716939937 51
4	D	3.43723396871777041008382193164489862422142367763 07
5	C	3.77073144615781997855778892842734867199554891785 43
6	B	4.44288293815836624701588099006069369861462168937 57
7	C	5.41991645432706565399912106672822149783245802990 99
8	D	5.80985767635318626426947322806264226896637429103 33
9	A	6.28318530717958647692528676655900576839433879875 02
10	D	7.10959048557161358103777053585384484182535018539 04
11	C	7.44389306692523896182785166002611046154626743425 93
12	B	8.88576587631673249403176198012138739722924337875 14
13	C	9.15688541405701741654222854052639985583098986080 10
14	D	9.31460464998877656090308499855652021252971490750 00
15	A	9.42477796076937971538793014983850865259150819812 53
16	C	11.03279675463843447133843889666073893657537403549 9
17	D	11.06995624407657986530390527322226040304650456079 1
18	A	12.56637061435917295385057353311801153678867759750 0
19	D	12.72562159345447828481470640457823632250127691771 4
20	C	12.94299624939872843440028072341137705714728149878 8

Table 2.4: Comparison of tritare eigenvalues for increasing Chebyshev interpolation points. The underlined digits agree with the exact values.

N	λ_1	λ_2	λ_3	λ_4	λ_5
8	1.7899303447995489	1.9965872857139577	3.1415925816836698	3.4372327838035917	3.7707264619751757
16	1.7899303735956240	1.9965873205689677	3.1415926535898993	3.4372339687176234	3.7707314461579373
32	1.7899303735947540	1.9965873205784181	3.1415926535895178	3.4372339687200064	3.7707314461579884
64	1.7899303735688430	1.9965873206931908	3.1415926535949552	3.4372339687623867	3.7707314461612293
Exact	1.7899303735955331	1.9965873205691058	3.1415926535897932	3.4372339687177704	3.7707314461578199
N	λ_6	λ_7	λ_8	λ_9	λ_{10}
8	4.4428828364677617	5.4197235271782480	5.8096656902252830	6.2833303992524243	7.1103059960011707
16	4.4428829381578971	5.4199164543224949	5.8098576763442571	6.2831853071825154	7.1095904857884245
32	4.4428829381622847	5.4199164543276348	5.8098576763563052	6.2831853071786208	7.1095904855732330
64	4.4428829381430379	5.4199164543172254	5.8098576763168399	6.2831853071619976	7.1095904856348522
Exact	4.4428829381583662	5.4199164543270656	5.8098576763531862	6.2831853071795864	7.1095904855716135
N	λ_{11}	λ_{12}	λ_{13}	λ_{14}	λ_{15}
8	7.4453223888012205	8.8859710674939585	9.1544903648618554	9.3107777477526135	9.4202831723709881
16	7.4438930675809791	8.8857658763206171	9.1568854134466733	9.3146046493771291	9.4247779614589930
32	7.4438930669253311	8.8857658763153431	9.1568854140571485	9.3146046499892492	9.4247779607692745
64	7.4438930669290295	8.8857658762693141	9.1568854140474407	9.3146046499530755	9.4247779607762290
Exact	7.4438930669252389	8.8857658763167324	9.1568854140570174	9.3146046499887765	9.4247779607693797
N	λ_{16}	λ_{17}	λ_{18}	λ_{19}	λ_{20}
8	11.0803489208057062	11.0956770376209537	12.7319695110709041	12.8567331736826311	13.0295790942384464
16	11.0327971666280469	11.0699564640382526	12.5663704008322537	12.7256207745053302	12.9429949317690891
32	11.0327967546381220	11.0699562440780390	12.5663706143585685	12.7256215934574115	12.9429962493994974
64	11.0327967546333863	11.0699562440961987	12.5663706143543035	12.7256215934561681	12.9429962494100312
Exact	11.0327967546384344	11.0699562440765798	12.5663706143591729	12.7256215934544782	12.9429962493987284

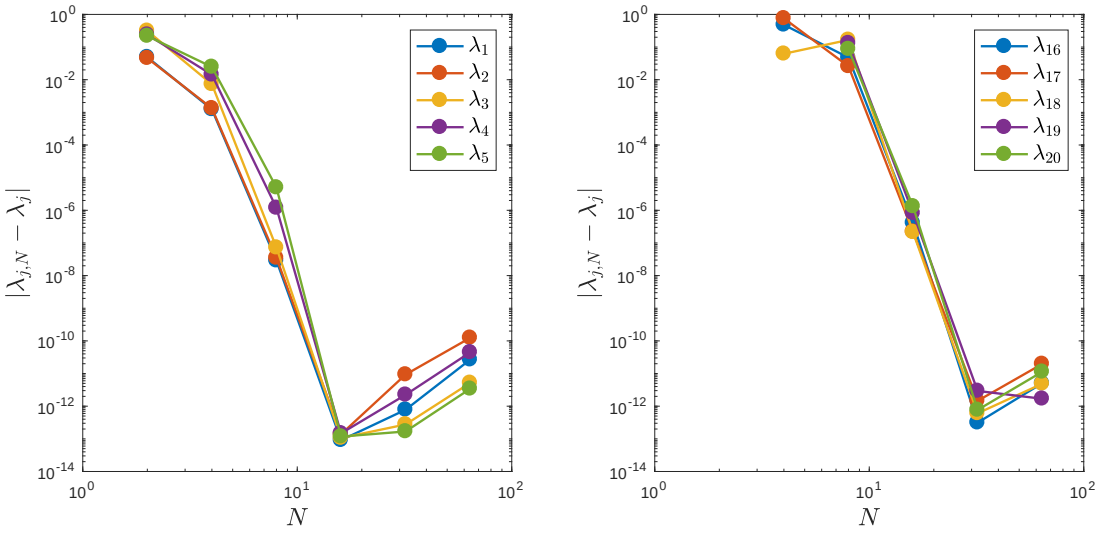

Figure 2.3: Convergence of the model as N increases, compared to the exact eigenvalues calculated in [4]: (left) eigenvalues $\lambda_1, \ldots, \lambda_5$; (right) eigenvalues $\lambda_{16}, \ldots, \lambda_{20}$. (Note that for $N = 2$, the model only computes the first 18 eigenvalues.)

2.4.3 The Tritare in $\mathbb{R}^3$

So far, we have only considered two dimensional strings with our model. We add an additional dimension for each string to test the model further, since real webs do not only vibrate in the 2D plane. Here we simply add a z component of 0 to each node of our tritare. In terms of the discretization, the z component contributes $N + 1$ additional rows and columns for each edge. We notice here that the third dimension adds new eigenvalues that are dispersed amongst those found in the 2D case. In Table 2.5 the eigenvalues repeated from the two dimensional case are starred.

Each eigenvalue produces its own eigenmode. These modes are depicted in Figures 2.5, 2.6, and 2.7, computed using $N = 16$. The original placement of the tritare is displayed in gray for each image. We show each eigenmode in a 3D view as well as in the x-y plane to help show the direction of movement as the tritare vibrates in each mode. Some of the modes,

Table 2.5: Computed eigenvalues of the tritare, allowing 3D vibrations. The stars denote eigenvalues that also appeared for the 2D model.

N	λ_1	λ_2 $\star$	λ_3 $\star$	λ_4 $\star$	λ_5
4	1.56967671	1.78869312	1.99525703	3.13432369	3.13432369
8	1.57079631	1.78993034	1.99658729	3.14159258	3.14159258
16	1.57079633	1.78993037	1.99658732	3.14159265	3.14159265
32	1.57079633	1.78993037	1.99658732	3.14159265	3.14159265

N	λ_6	λ_7 $\star$	λ_8 $\star$	λ_9 $\star$	λ_{10}
4	3.13432369	3.42303000	3.74612956	4.43260308	4.59487016
8	3.14159258	3.43723278	3.77072646	4.44288284	4.71225228
16	3.14159265	3.43723397	3.77073145	4.44288294	4.71238898
32	3.14159265	3.43723397	3.77073145	4.44288294	4.71238898

specifically those corresponding to λ_4, λ_5, and λ_6, display movement in the three dimensional plane. Several of the others shift only in a two dimensional plane. In Figure 2.6, λ_9 is of special note. The images shown appear to not have displacement in any direction, however, the tritare is vibrating in the x-y plane in this case. Over time the strands are shaking forward and backwards along their current position. This movement can be seen by the bunching of the Chebyshev points to alternating ends of each strand. As λ increases, the frequency increases, leading to the more interesting dynamics of the tritare network displayed in Figure 2.7. The lower eigenvalues, however, represent the more dominant movements that occur naturally in the network.

Figure 2.4 shows the distribution of the eigenvalues. Notice the existence of repeated eigenvalues that occur when considering movements in $\mathbb{R}^3$ but do not occur in $\mathbb{R}^2$. The eigenmodes that correspond to these repeated eigenvalues are very similar to each other. (MATLAB's eigensolver is picking three linearly independent vectors that span the three dimensional eigenspace.) The first repeated eigenvalue occurs at $\lambda_4 = \lambda_5 = \lambda_6 = \pi$; the eigenmodes for each of these can be seen in Figure 2.5. The eigenvalues with multiplicity greater than one

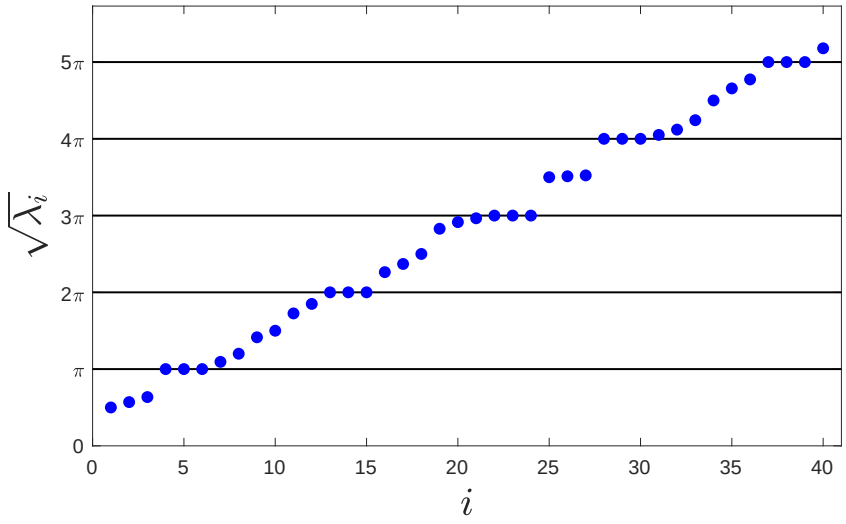

Figure 2.4: Distribution of the first 40 eigenvalues of the 3D tritare.

occur at multiples of π. Figure 2.7 shows the second repeated eigenvalue at $2\pi \approx 6.2832$, which occurs at λ_{13}, λ_{14}, and λ_{15}. Again the movements of these three eigenvalues are quite similar. Note the increased frequency of the waves occurring on each string in the eigenmodes between $\lambda_i = \pi$ and $\lambda_j = 2\pi$.

2.5 The General Case

Our goal from here is to apply the discretization (described for the two-string and tritare examples) to larger networks of strings. The complexity will increase with each additional string and boundary/interior condition we add to our model, and with the fact that our web vibrates in three dimensions. For each additional string added to the network, **A** and **B** grow to accommodate the string's eigenvalue problem, boundary, slope, and continuity

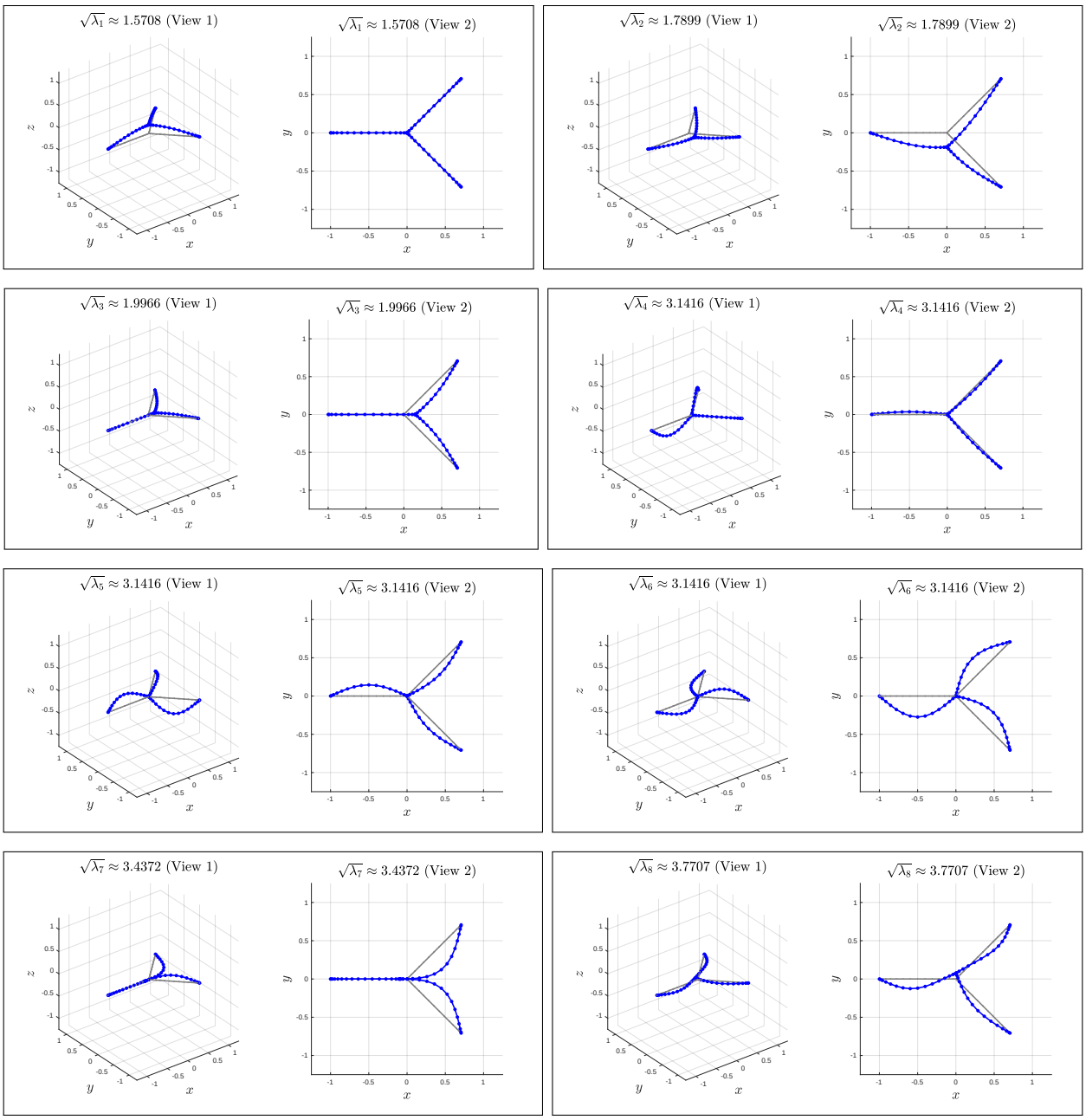

Figure 2.5: Eigenmodes for $\lambda_1, \ldots, \lambda_8$. Each mode is shown in a 3D view and in the x-y plane. The original position is displayed in gray in each image. Note the placement of the points along each strand (bunching implies movement along the strand towards that end).

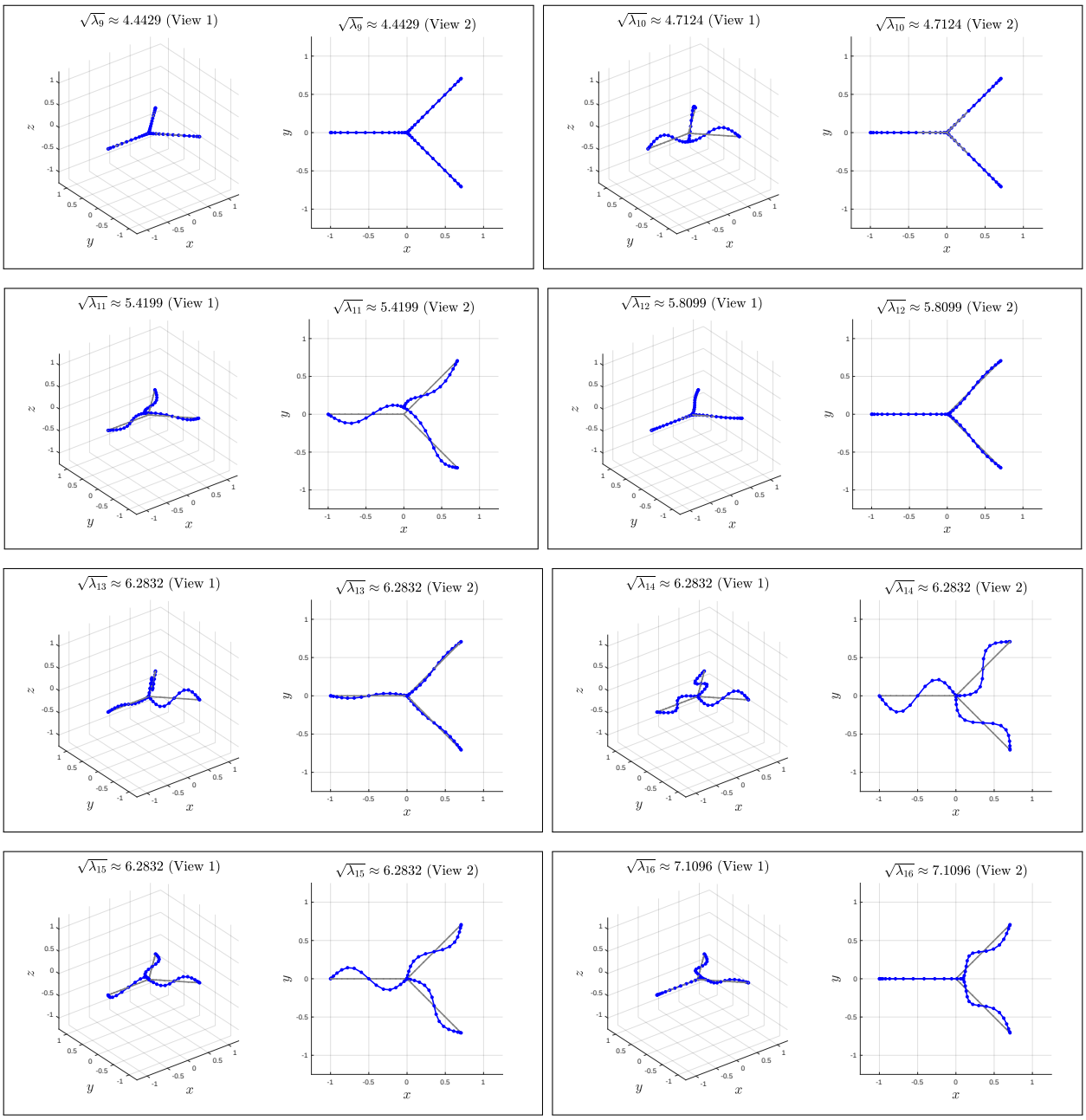

Figure 2.6: Eigenmodes for $\lambda_9, \ldots, \lambda_{16}$. Each mode is shown in a 3D view and in the x-y plane. The original position is displayed in gray in each image. Note the placement of the points along each strand (bunching implies movement along the strand towards that section of the string).

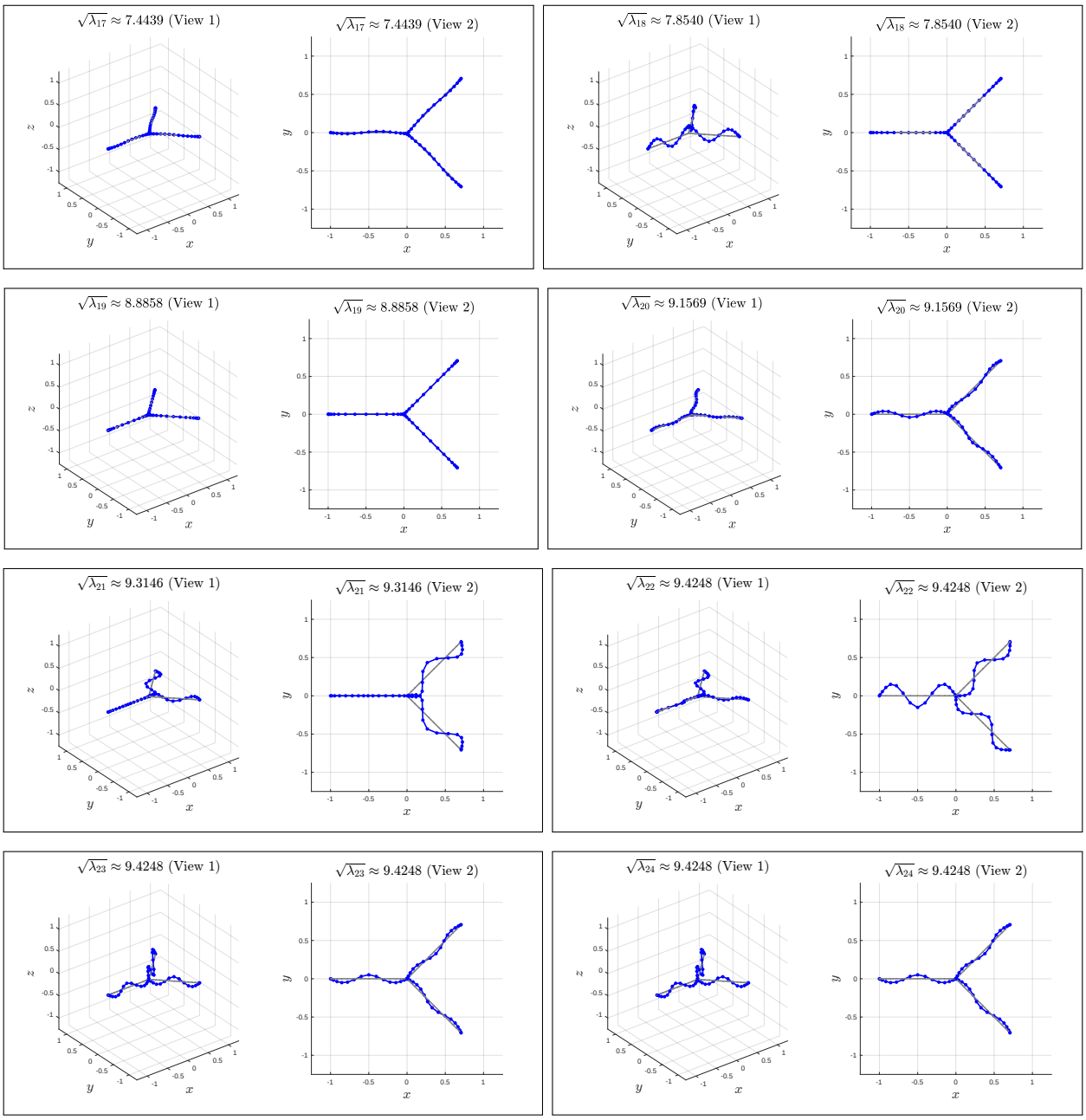

Figure 2.7: Eigenmodes for $\lambda_{17}, \ldots, \lambda_{24}$. Each mode is shown in a 3D view and in the x-y plane. The original position is displayed in gray in each image. Note the placement of the points along each strand (bunching implies movement along the strand towards that section of the string).

conditions. In general, $\mathbf{A},\ \mathbf{B} \in \mathbb{R}^{m\times m}$ where

$$m = 3(N+1)n, \tag{2.16}$$

where n equals the number of strings. Since we are considering the x, y, and z components of each string, each string will contribute $3(N+1)$ rows and columns to the discretization matrix. With each additional string, the boundary and continuity conditions will contribute to the discretization matrix $\mathbf{A}$ in the same manner as described for the two-string case. The slope condition proves more interesting. For each interior node, the slope condition incorporates every string attached to the node. Denote η as a single node, then let $\mathcal{J}(\eta) = \{i\text{th string} \ : \ \mathbf{r}^i(s_j,t) = \eta\}$ where $s_j = 0$ or $s_j = \ell^i$. In general, we describe the slope condition as

$$\sum_{i\in\mathcal{J}(\eta)} \epsilon^i(\eta)\mathbf{P}^i\mathbf{r}^i_s(s_j,t) = 0, \tag{2.17}$$

where $\epsilon^i = 1$ when, for string i, $s_j = 0$ and $\epsilon^i = -1$ when $s_j = \ell^i$. To complete this condition in the discretization requires zeroing out the corresponding rows of $\mathbf{B}$.

Given any network of strings that satisfies our boundary conditions, we can implement the discretization. We then use the eigenvalues and vectors of the generalized eigenvalue problem outlined above to plot the dynamics of each eigenmode. For large N and/or large webs, we do not compute all eigenvalues of (2.11). In the interest of saving computational time, we use the `eigs` function in MATLAB, which allows the user to specify the number of eigenvalues to calculate. This routine uses the ARPACK software package, based on the implicitly restarted Arnoldi method [10]. We call `eigs` with the '`sm`' flag, which computes the smallest magnitude eigenvalues essentially by applying the implicitly restarted Arnoldi method to $\mathbf{A}^{-1}\mathbf{B}$. To our specific eigenvalue problem, we require the smallest eigenvalues, since $\sqrt{\lambda}$ represents the frequency of vibration of the network of strings, and we expect the

dominant movements of a vibrating spider web to correspond to the lower frequencies, and thus the lower eigenvalues. The next chapter will put this idea to the test on much larger systems corresponding to regular web-like networks.

Chapter 3

Regular Webs

This chapter applies the model and discretization described in Chapter 2 to study the vibrations of *regular* webs. These are webs one might draw for a Halloween decoration, with radial symmetries about the center; each section of the radial strands are the same length. These webs provide a uniform environment for preliminary studies of the discretization.

3.1 Regular Web Structure

Given r radial strands, we create a regular web structure with the radial strands separated by angle $2\pi/r$. Beginning with a single center node, given a length, ℓ, and number of layers, d, we place d nodes on each radial strand at increments of length ℓ, including a common node at the center of the web. Each interior node then connects to the corresponding interior node on both adjacent radial strands. This system results in a uniform web with $d-1$ rings around the center of the web. In this chapter we display and analyze the dynamics of three different regular webs, shown in Figure 3.1. These three webs allow us to study how the dynamics and eigenvalues vary with the structure of the web. Note that each web is scaled to

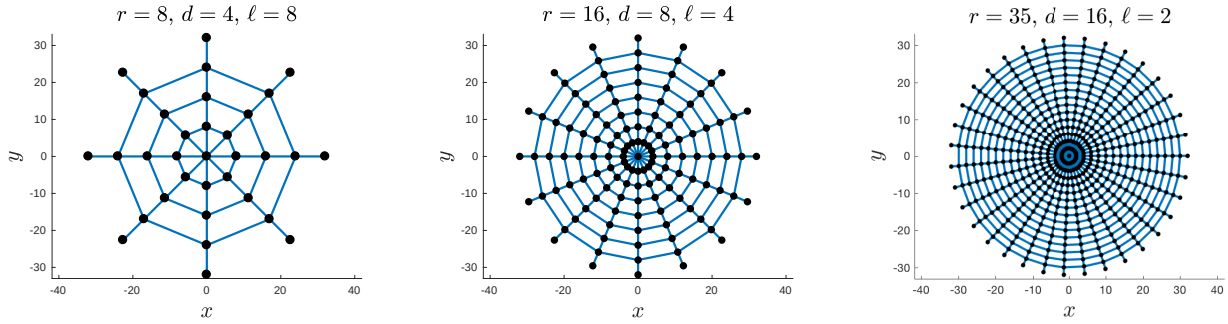

Web 1 Web 2 Web 3

Figure 3.1: Three regular webs.

have the same total radius about the center. We made this choice so Webs 1, 2, and 3 have comparable size to that of the real web analyzed in Chapter 4. In addition to the similar structures for each web, we assume homogeneity of the material properties of each string. Thus we assume that each string, whether radial or spiral, has the same cross sectional area, stiffness, and density. We set $\rho^i = k^i = 1$ and $\sigma^i = 2$ for all i, for simplicity.

3.2 Eigenvalues

3.2.1 Convergence

We first analyze the convergence of the algorithm by comparing the computed eigenvalues for varying values of N, the number of Chebyshev points used for each string. We compute the eigenvalues for Webs 1, 2, and 3 for $N = 2, 4, 8, 16, 32$, and 64. Figures 3.2, 3.3, and 3.4 below compare the eigenvalues for each N against those computed for $N = 64$. Based on our comparison of the model's computed eigenvalues to the exact eigenvalues for the tritare (Section 2.4.1), we may again lose accuracy with $N = 64$. However, the purpose of this

analysis is to show that as N increases, the computed eigenvalues begin to converge to the same number; thus we still consider $N = 64$ as closest to the exact value. Each convergence plot displays the same overall trend despite the specific structure of the web. Each web shown has $\lambda_2 = \lambda_3$ and $\lambda_4 = \lambda_5$. Note also the rate at which the algorithm gains accuracy; for example, consider λ_5 in Figure 3.3. When $N = 4$ the eigenvalue is computed to 6 digits of accuracy, but with $N = 8$ we gain 6 more digits of accuracy. This behavior is consistent with the "spectral accuracy" often exhibited by Chebyshev pseudospectral methods [20]. For each web, we obtain at least 12 digits of accuracy with $N = 16$ in all of the displayed eigenvalues. We report the smallest eigenvalues $(\lambda_1, \ldots, \lambda_5)$ and some slightly larger eigenvalues $(\lambda_{15}, \ldots, \lambda_{20})$ for each web. The discretization $N = 16$ appears to give the most accuracy for each of the webs' displayed eigenvalues with the exception of λ_1, λ_2, and λ_3 in Figure 3.8, which are closest to the "exact" eigenvalue when $N = 4$. Since little to no accuracy is gained from computing the eigenvalues for $N = 64$, we conclude that $N = 16$ or perhaps even $N = 32$ provides a sufficient level of accuracy. (If we sought eigenvalues deep in the interior of the spectrum, larger values of N would be justified.)

3.2.2 Distribution

As mentioned previously, the frequency of vibration is represented by $\sqrt{\lambda_i}$, where λ_i is an eigenvalue of the generalized eigenvalue problem (2.11). Figure 3.5 displays the distribution of these frequencies for Webs 1, 2, and 3. The reported frequencies for each web follow a very similar pattern despite changes from web to web. For each web, we see several eigenvalues with algebraic multiplicity 2 or even 3, a result of the planar nature of the web and its geometric symmetries. There are consistent groupings between the eigenvalues of each web of repeated or very close eigenvalues. Note that the first six eigenvalues agree closely across the three different webs. Deeper into the spectrum, we begin to see more

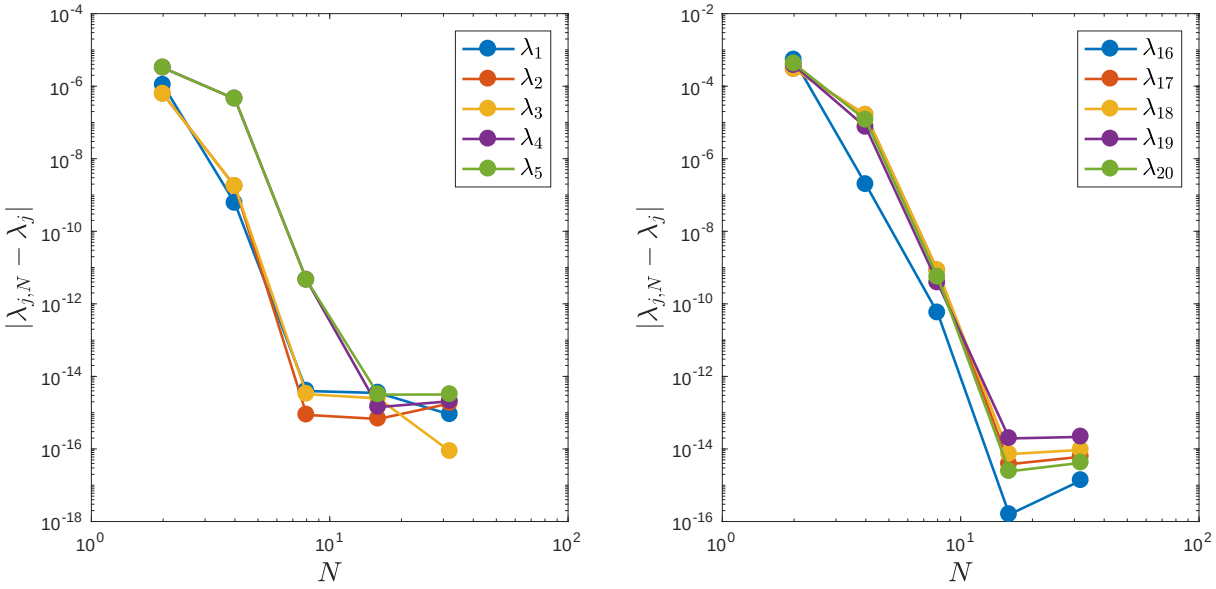

Figure 3.2: Convergence of eigenvalues for Regular Web 1, using $N = 64$ for the "exact" eigenvalues, showing $\lambda_1, \ldots, \lambda_5$ (left) and $\lambda_{16}, \ldots, \lambda_{20}$ (right).

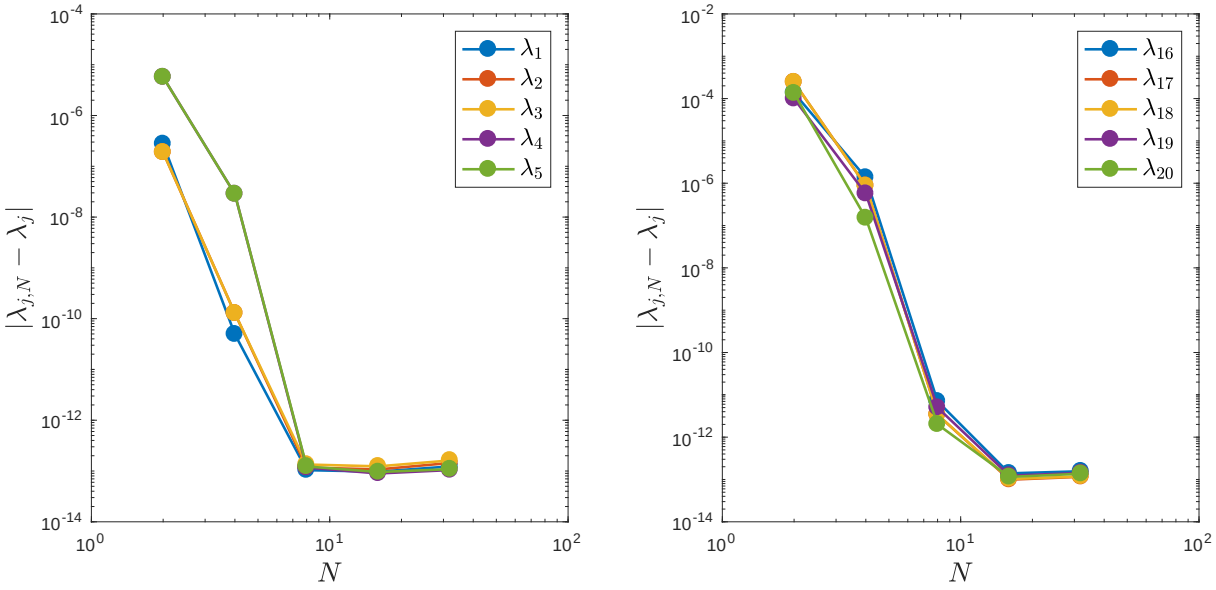

Figure 3.3: Convergence plots for Regular Web 2, using $N = 64$ for the "exact" eigenvalues, showing $\lambda_1, \ldots, \lambda_5$ (left) and $\lambda_{16}, \ldots, \lambda_{20}$ (right).

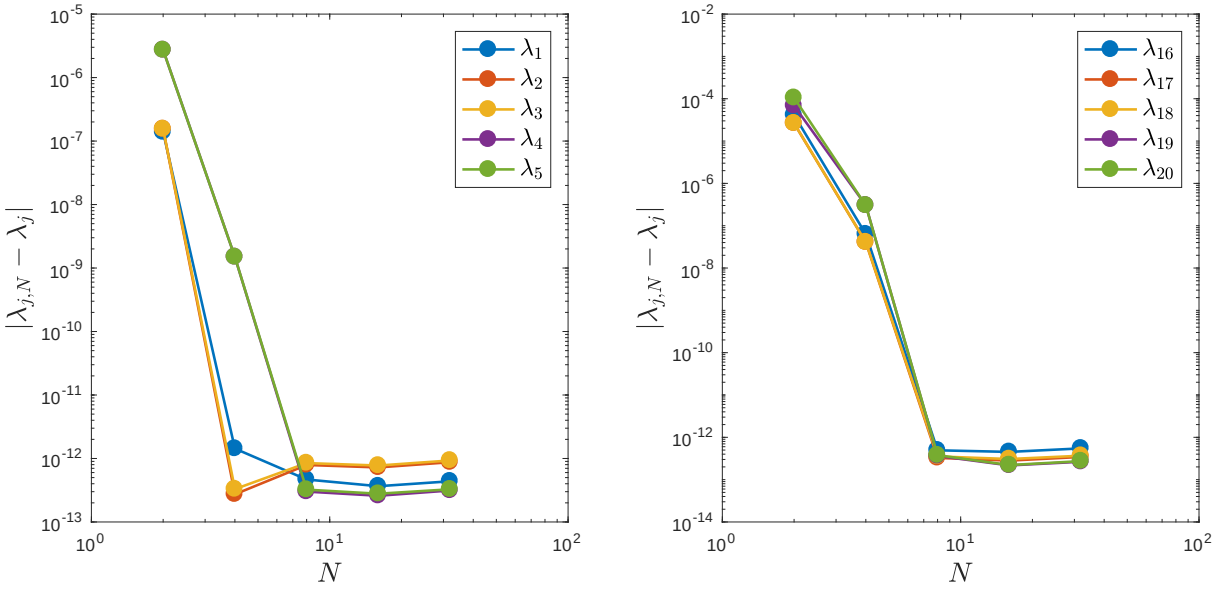

Figure 3.4: Convergence plots for Regular Web 3, using $N = 64$ for the "exact" eigenvalues, showing $\lambda_1, \ldots, \lambda_5$ (left) and $\lambda_{16}, \ldots, \lambda_{20}$ (right).

differentiation between the three webs, with Web 3 having the largest eigenvalues. Even with the separation of values towards the higher end of the spectrum, the frequencies for each web continue to follow similar patterns.

3.3 Dynamics of Uniform Regular Webs

Using our model, we visualize the movements of the first ten eigenmodes for Webs 1, 2, and 3. For every eigenmode, we display a three dimensional and x-y plane view of the movement. This set up helps us to visualize when the eigenmodes are moving in plane. The eigenvalues were computed with $N = 16$ for each web; thus each dot along the strings corresponds to a Chebyshev point. We analyze the eigenmodes of each web and compare the similarities between them.

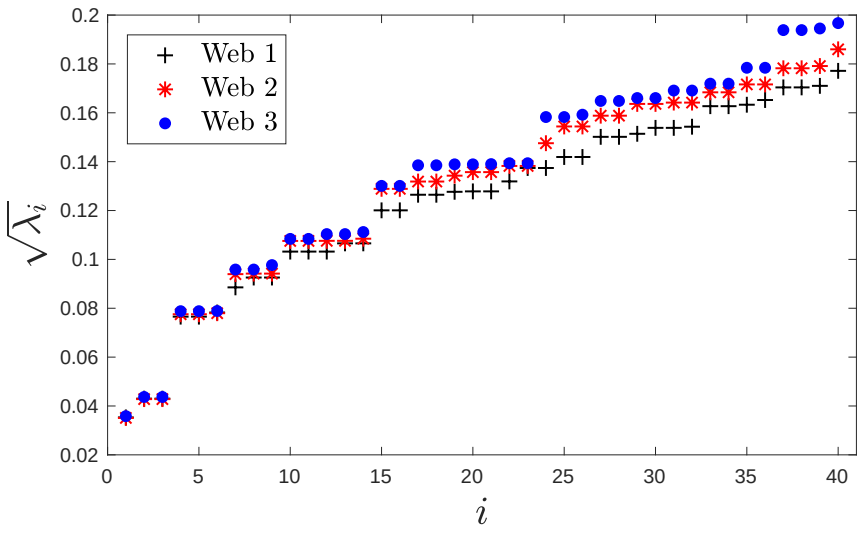

Figure 3.5: Comparison of smallest 40 eigenvalues for Regular Webs 1, 2, and 3

3.3.1 Web 1 Dynamics

The frequencies of vibration for each eigenmode are reported with each image in Figure 3.6. The discretization matrices **A** and **B** have dimension 2856×2856 for Web 1, which has 33 nodes and 56 strings. Note that four of the ten reported eigenmodes do not shift in the x-y plane (λ_1, λ_4, λ_5, and λ_7). There are three sets of repeated eigenvalues that occur in the first ten: $\lambda_2 = \lambda_3$, $\lambda_4 = \lambda_5$, and $\lambda_8 = \lambda_9$. Individual pairs exhibit similar eigenmodes that vibrate in the same manner, but typically in different directions. For $\lambda_2 = \lambda_3$, both modes shift the center node close to an edge of the web, squishing strings in the shifted direction and stretching the other side to accommodate this movement (which occurs strictly in the x-y plane). In contrast, λ_4 and λ_5 vibrate solely in the z direction and tilt in opposite directions, but in a very similar manner. The eigenmodes for λ_8 and λ_9 also exhibit similar movements. They both squish towards the center of the web, however on different axes in the x-y plane. Also λ_6 is of special note, as its mode causes the web to twist in plane.

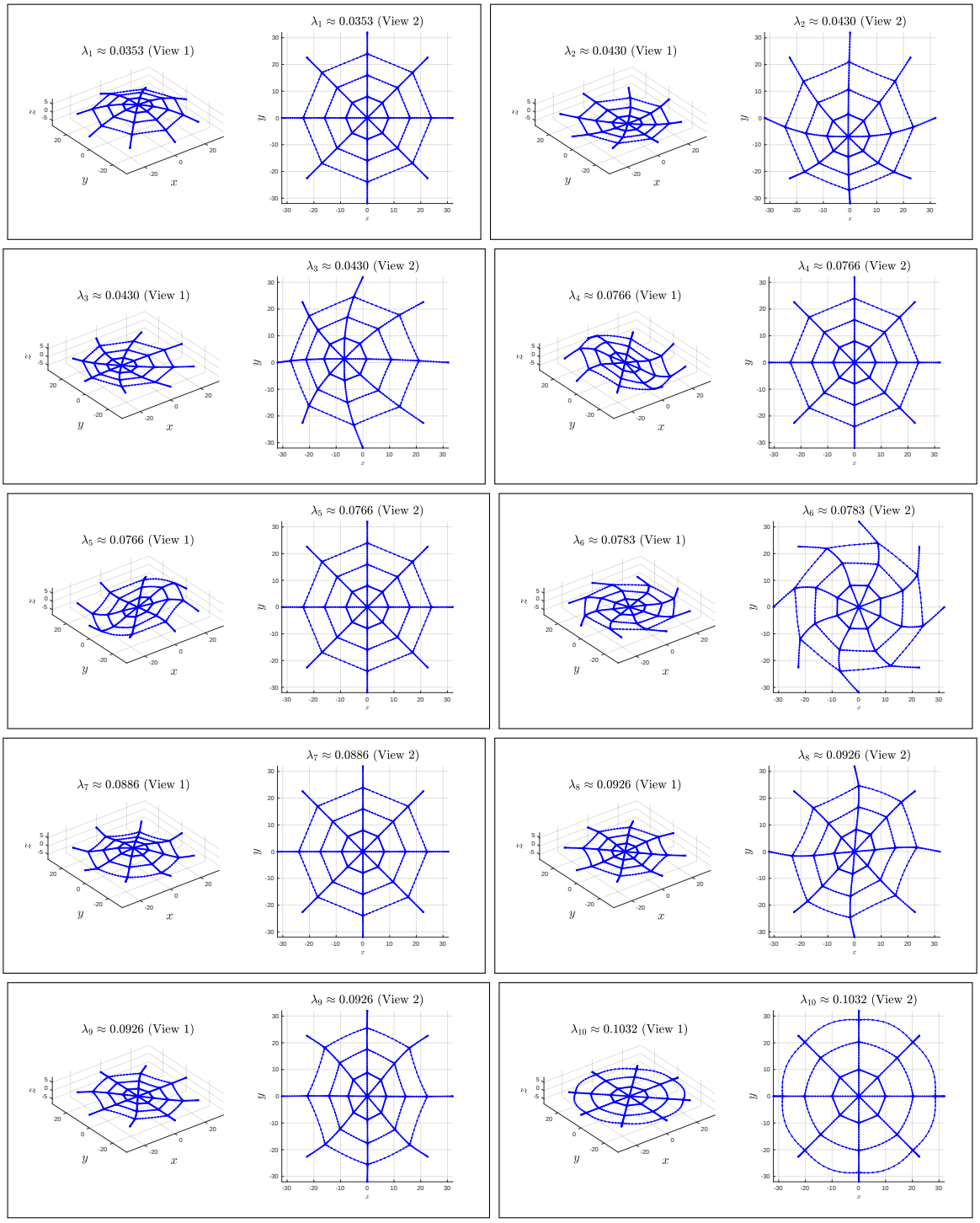

Figure 3.6: Eigenmodes for Regular Web 1 with 8 radial spokes and 4 layers.

3.3.2 Web 2 Dynamics

The eigenmodes of Web 2 are also computed using $N = 16$ and shown in Figure 3.7. Web 2 has 129 nodes and 240 strings; giving discretization matrices $\mathbf{A}$ and $\mathbf{B}$ of dimension 12240×12240. Examining the eigenmodes depicted in Figure 3.7, we see many similarities between these and those for Web 1 in Figure 3.6. As before, the first eigenmode causes oscillations up and down with no variation in the x-y plane. This dominant mode has the lowest frequency at $\sqrt{\lambda_1} \approx 0.1405$ and has the simplest movement. This eigenmode resembles the single sine wave solution expected as the dominant eigenmode for a single string. Each eigenmode for Web 2 closely resembles those of Web 1 except for λ_{10}. Here the tenth eigenmode shifts the innermost ring, while for Web 1 it appears as if each spiral string is expanding outward with no movement of the radial strands. Note that again there exist repeated eigenvalues at $\lambda_2 = \lambda_3$, $\lambda_4 = \lambda_5$, and $\lambda_8 = \lambda_9$. Here again, the sixth eigenmode also twists in the x-y plane.

3.3.3 Web 3 Dynamics

Figure 3.8 shows the eigenmodes for our final regular web with uniform properties. This web resembles the traced orb web in Chapter 4 in size and number of nodes; however, its highly regular structure and material properties cause significant variations from the traced web. These similarities and differences will be discussed further in Chapter 4. Again we compute the eigenvalues and vectors for Web 3 using $N = 16$. At 561 nodes and 1085 strings, we solve equation (2.11), where $\mathbf{A}$ and $\mathbf{B}$ have dimensions 55335×55335. Note again that λ_1 corresponds to the single sine wave on the entire system. The first eigenmode in Figures 3.6, 3.7, and 3.8 all exhibit drum-like movement, oscillating up and down in the z direction. Again note the similarity between eigenmodes corresponding to $\lambda_1, \ldots, \lambda_6$ between Webs 1,

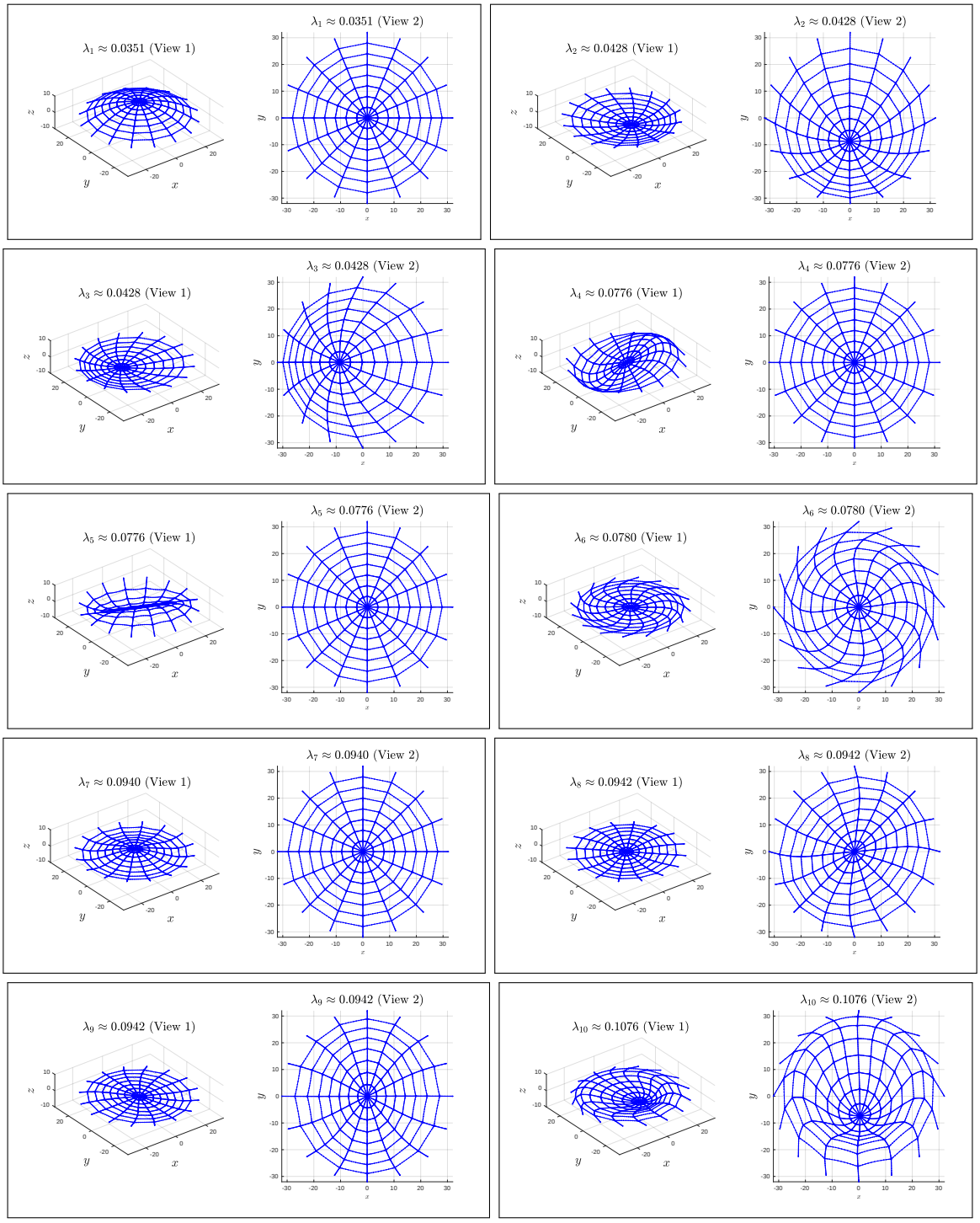

Figure 3.7: Eigenmodes for Regular Web 2 with 16 radial spokes and 8 layers.

Table 3.1: Average computing time and wall-clock time, as reported by MATLAB, averaged over 5 runs that each compute the 20 smallest eigenvalues on each web. Times are reported in seconds.

Avg Time	Web 1	Web 2	Web 3
Dimension	2856×2856	12240×12240	55335×55335
cpu	43.62	1053	25324
wall-clock	1.46	21.27	484.99

2, and 3. Web 3 again has a third repeated eigenvalue as the other webs do, however, in this case it occurs at $\lambda_7 = \lambda_8$. The corresponding eigenmodes closely resemble those of λ_8 and λ_9 for Webs 1 and 2. For Web 3, λ_9 now closely resembles λ_7 for Web 1 and Web 2. Again, λ_{10} differs greatly from λ_{10} for both Web 1 and Web 2. For Web 3, the tenth eigenmode does not shift in the x-y plane at all, while for both of the other webs the tenth mode does shift.

The high regularity of the three webs yields consistent results for the eigenvalues and eigenmodes, as can be seen in Figures 3.6, 3.7, and 3.8, as well as in the eigenvalue distributions shown in Figure 3.5. There is indeed slight variation between the modes in each of the webs displayed; however, the eigenvalues remain in similar groupings for all three webs and the eigenmodes produce very similar movements. The increase of nodes and strings, while not having a dramatic effect on the eigenvalues, does affect the time taken to solve the generalized eigenvalue problem. Table 3.1 compares the average computational time (measured by MATLAB's `cputime` function) and wall-clock time (measured by MATLAB's `tic` and `toc` function calls) taken to compute 20 eigenvalues of equation (2.11) for Webs 1, 2, and 3 when $N = 16$. These values correspond to the time taken for the function call `eigs` in MATLAB, when run on a machine made up of 4 Intel 15 core 2.8 GHz processors. The machine contains a total of 1TB of RAM. Notice the dramatic increase in time taken to compute the eigenvalues as the webs increase in number of nodes and strings.

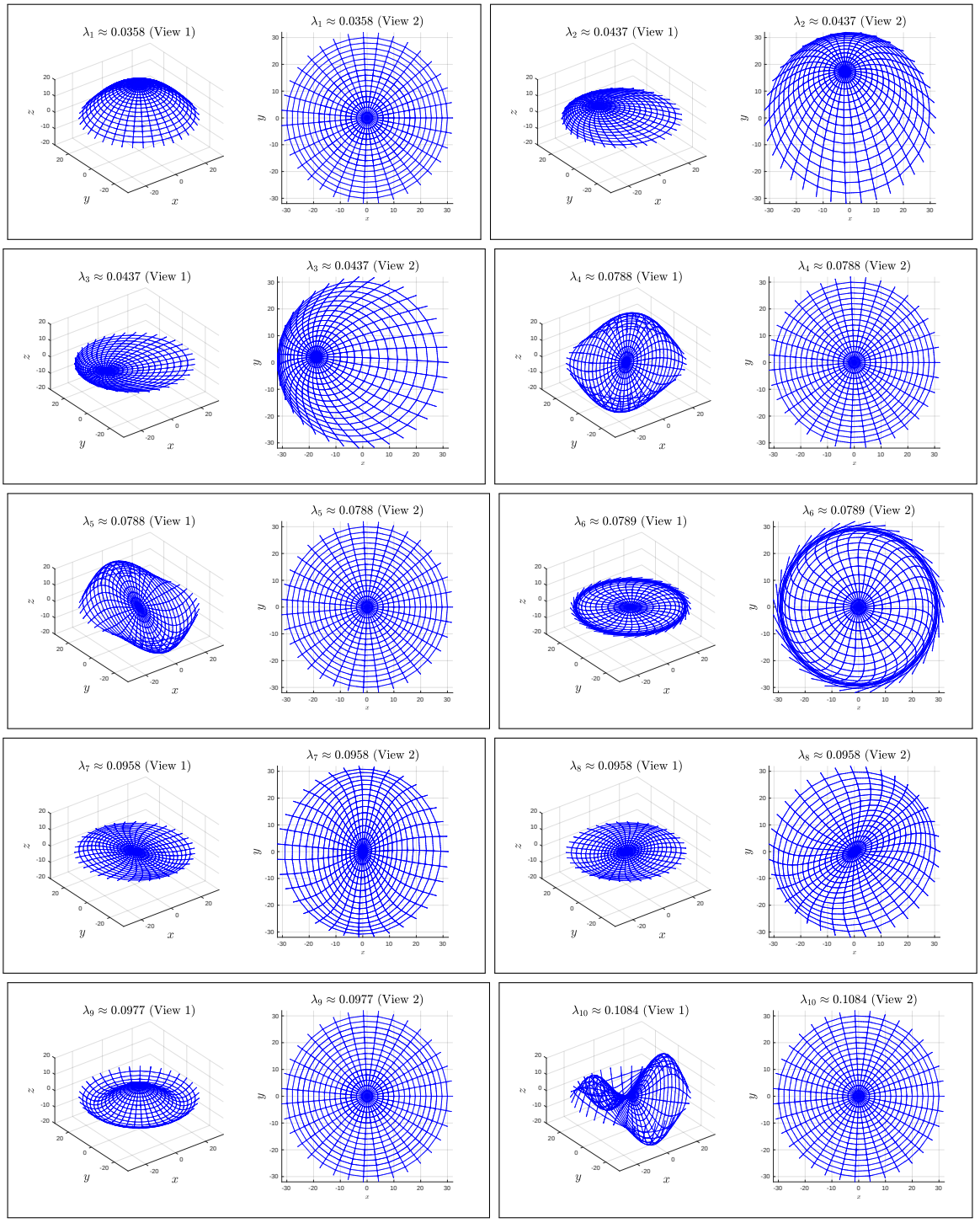

Figure 3.8: Eigenmodes for Regular Web 3 with 35 radial spokes and 16 layers.

Chapter 4

Realistic Webs

To further explore the validity of the model and investigate the biological applicability of this tool, we transition to realistic webs. The previous examples in Chapter 3 provide a great vehicle to study the accuracy and convergence of the model. However, in the wild, spiders do not create perfectly uniform webs. How do real spider webs vibrate?

4.1 Tracing Real Webs

To analyze the vibrations of a real web, we must input the necessary characteristics (junctions and adjacencies) of said web into the model. To quantify each silk strand and connection that occurs in the web, the model requires the coordinates of each junction within the web (nodes) and an adjacency list of strings. Given a picture of a real web, we record the coordinates of each junction and which strands connect at that junction. To trace this structure we developed a script in MATLAB to allow a user to identify node locations via mouse click, based on a pixelated image of the web. To maintain realistic web size, we account for the length of each edge by scaling the pixel coordinates collected to match the reported physical

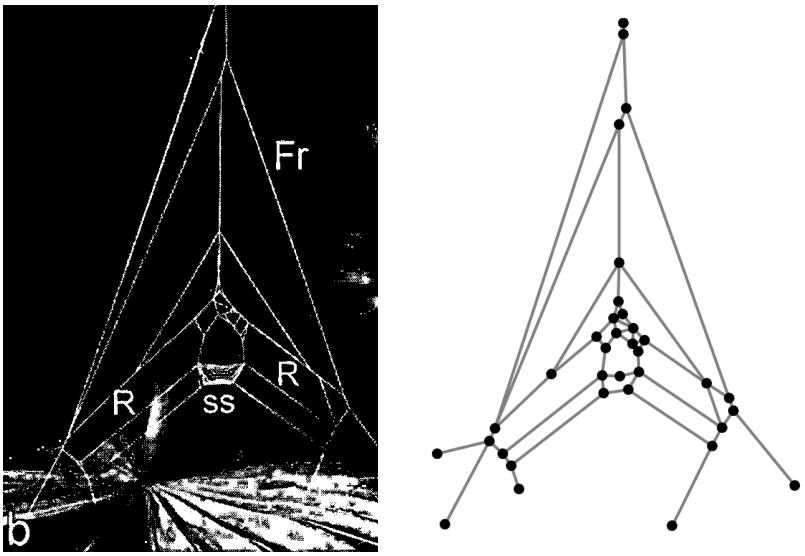

Figure 4.1: (left) Image of a real web from [5, p. 184] used to trace nodes and edges. (right) Traced image with nodes junctions marked.

scale for the web. If no scale is reported, we attempt to estimate realistic lengths for each strand.

When tracing a web, accuracy is limited by the number of pixels in the image. Note this limitation in Figure 4.2; not all of the strands were able to be traced due to the tolerance required to determine the difference between new node locations and one previously stored. As a result, the left-hand image has many more spiral strands than our traced version; however, the overall appearance of the web is maintained with our traced version. Further work could improve the accuracy of the traced webs. We begin analysis with uniform material properties for all strings within in a web; when accounting for the material differences between radial and spiral strands, we must additionally characterize each strand as either radial or spiral. We first trace a simple real web in order to test the model on a non-regular web; see Figure 4.1. This web, found in [5], belongs to a *Deinopis* spider. This incomplete web has distinct features of an orb web, as one can see the frame and radial threads. To test an actual orbweaver web, we traced a web of an *Agriope trifasciata*, as shown in Figure 4.2.

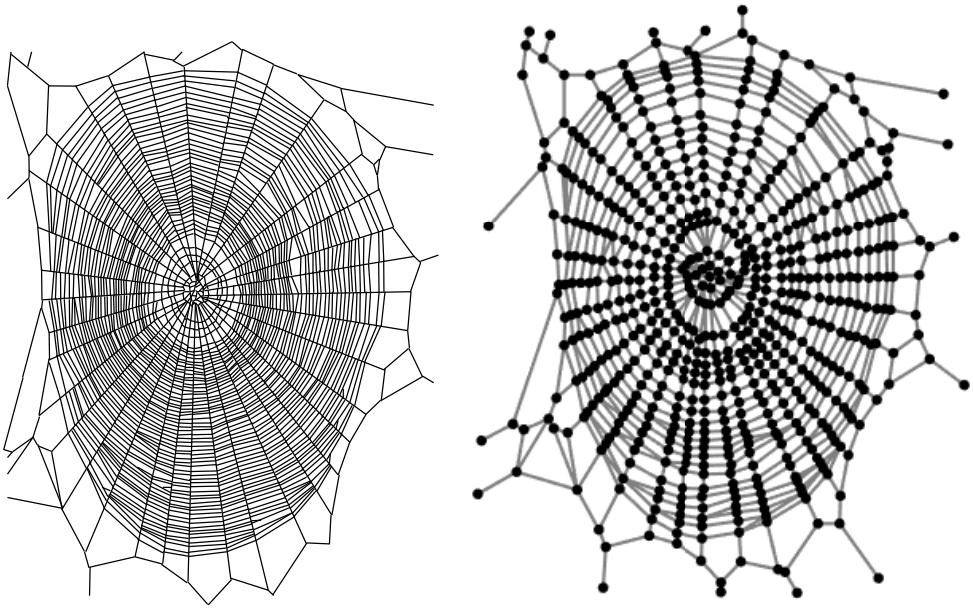

Figure 4.2: (left) Image of an orb web taken from [19]. (right) Traced version. Each stored node is denoted by a black dot and each string by a gray line.

4.2 Dynamics for Uniform Material Properties

After tracing the two webs above, we apply the discretization from Chapter 2 to both webs. We traced the web in Figure 4.1 as an initial proof of concept for a non-regular web. Figure 4.4 displays the first 10 eigenmodes for this simple network. For both realistic webs, we set $\sigma^i = 2$, $k^i = 1$ kg·cm/s^2, and $\rho^i = 1$ kg/cm. These modes are computed using $N = 16$. This web has 35 nodes and 53 strings, resulting in $\mathbf{A}$ and $\mathbf{B}$ having dimension 2703×2703. Figure 4.3 shows the nonzero elements of both $\mathbf{A}$ and $\mathbf{B}$. When constructing $\mathbf{A}$ and $\mathbf{B}$ we first account for the eigenvalue problem in equation 2.10. Thus the first several thousand rows allocated correspond to labels (3) and (7) in Table 2.1. Note that the only nonzero elements of $\mathbf{B}$ correspond to the eigenvalue condition, while the boundary, slope and continuity conditions accounted for last have corresponding rows of all zeros in $\mathbf{B}$. The dynamics of this web are shown in Figure 4.4, where the original location of the web is displayed in gray to

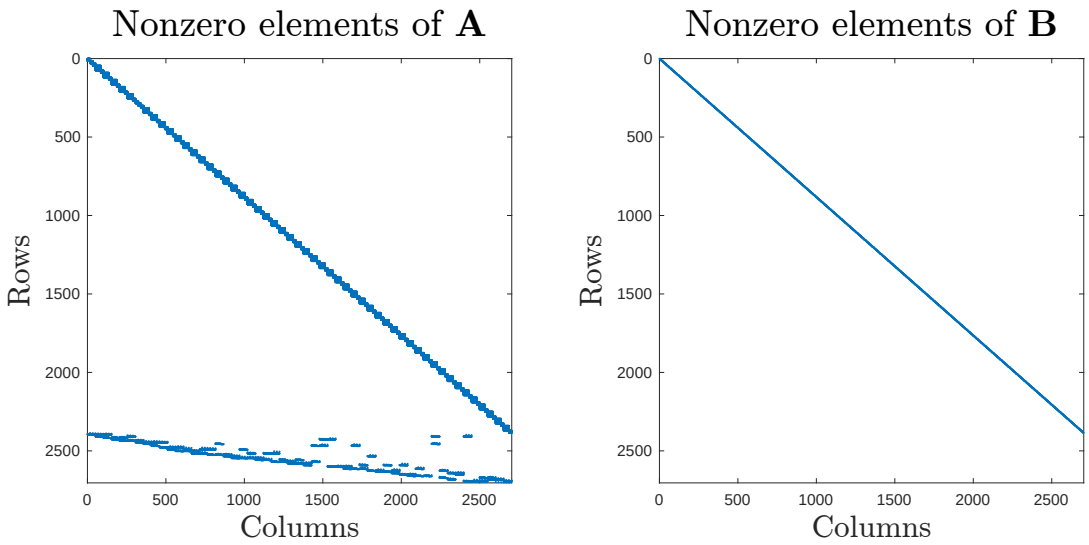

Figure 4.3: Nonzero elements for discretization matrices **A** and **B** for the web in Figure 4.1.

help show the displacement of the web within each eigenmode. The first eigenmode oscillates strictly in the z direction. This drum-like behavior resembles that of the regular webs shown in Chapter 3. For λ_2, we see the entire web shifted to the side similar to the movements of λ_2 and λ_3 in Figures 3.6, 3.7, and 3.8. A distinct difference between these eigenvalues and those of the regular webs is that there are no longer eigenvalues with algebraic multiplicity greater than 1. Many of these eigenvalues are clustered close together as before, but the lack of strict symmetry in the system alters the dynamics.

4.2.1 Orb Web

Analyzing the uniform dynamics of the orb web traced in Figure 4.2, we obtain the eigenmodes shown in Figure 4.5. This figure shows the first 10 eigenmodes. This web has 633 nodes and 1241 edges. Thus our discretization matrix as described in Chapter 2, when $N = 16$, has dimension 63291×63291. (The length of each side is calculated by equation (2.16): $3\times(16+1)\times 1241 = 63291$. The bulk of the computational time occurs during the call

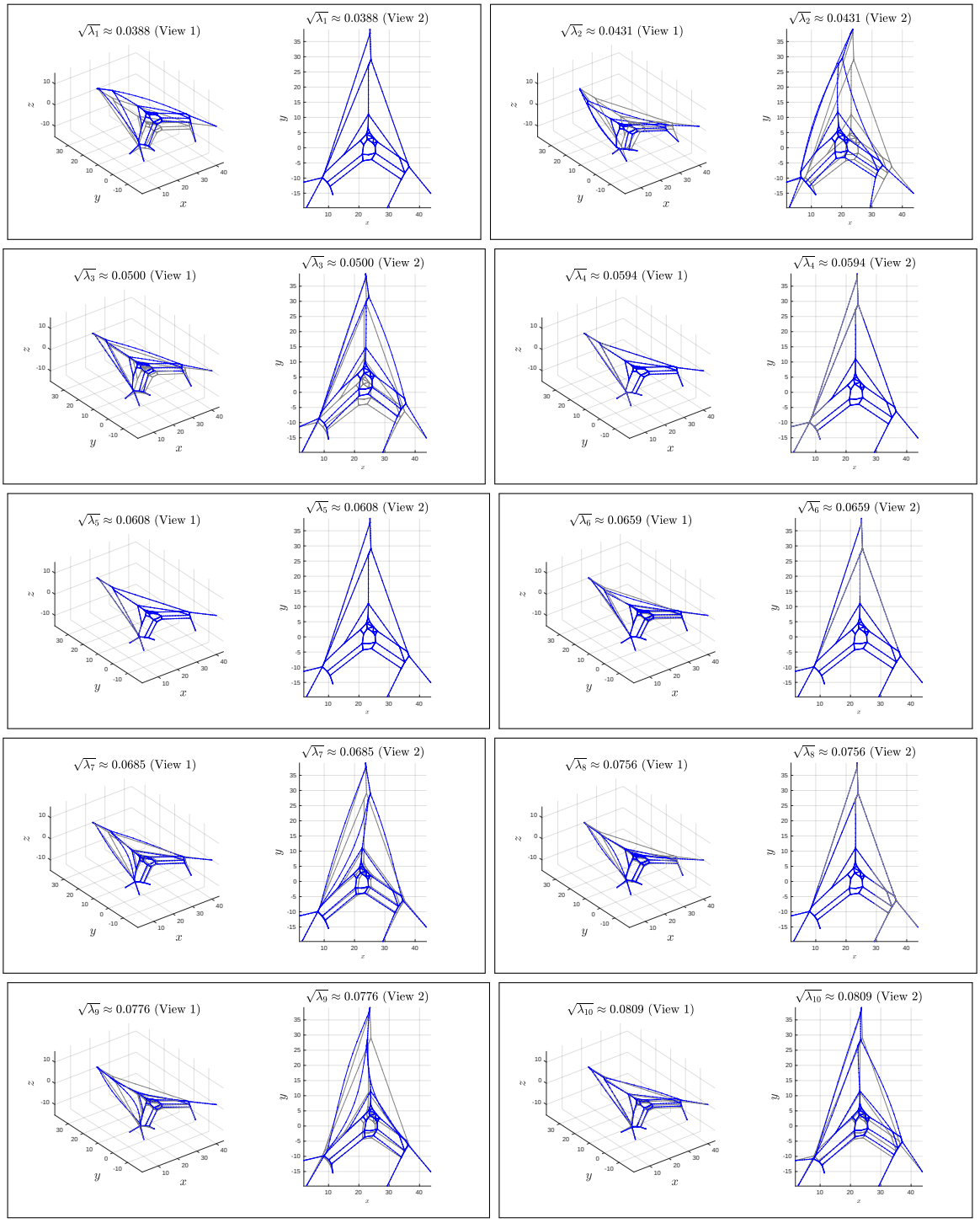

Figure 4.4: Eigenmodes for the real web as shown in Figure 4.1.

to `eigs`. The average `cputime` to compute the eigenvalues is 41589 seconds over five runs, seeking 20 eigenvalues with $N = 16$. The average wall-clock time of the eigenvalue computation of those same five runs is 910.14 seconds. Another possible concern for the speed of the algorithm occurs during the construction of $\mathbf{A}$ and $\mathbf{B}$. In this case, we are constructing two 63291×63291 dimensional matrices using sparse matrix techniques; however, this cost is negligible compared to the eigenvalue computation. Once again, the first eigenmode gives drum-like motion, as seen in each regular and the earlier traced web. The modes for λ_2 and λ_3 resemble those of Figure 3.8, with the entire web shifting in the x-y plane. Also note the "squishing" patterns of λ_7, λ_8 and λ_9 that resemble those of the regular webs. As with Figure 4.4, we do not see double eigenvalues for this large realistic web. We do, however, see similar clustering of two to four eigenvalues, as with the regular webs. Figure 4.6 shows the distribution of the eigenvalues for the orb web. Notice the relatively large jump between eigenvalues that occurs between λ_3 and λ_4.

The dynamics of the orb web differ from those of the regular webs in Chapter 3 in several ways. The irregularity of the orb web does not allow for the repeated eigenvalues seen in the regular webs. Additionally, the movements within the orb web are less symmetric than they previously seem. Despite these differences, with homogeneity of all the strings within the web, we see similar dynamics and distribution of eigenvalues for the orb web and Regular Webs 1, 2, and 3. The regular webs also exhibit the large jump between λ_3 and λ_4 that is seen in the orb web (compare Figures 3.5 and 4.6). Additionally, we see clustering of three or four eigenvalues with the orb web as well, but in this case they are less distinct. In Figure 3.5, the separation between clusters is more distinct since one or more of each cluster is often a repeated eigenvalue.

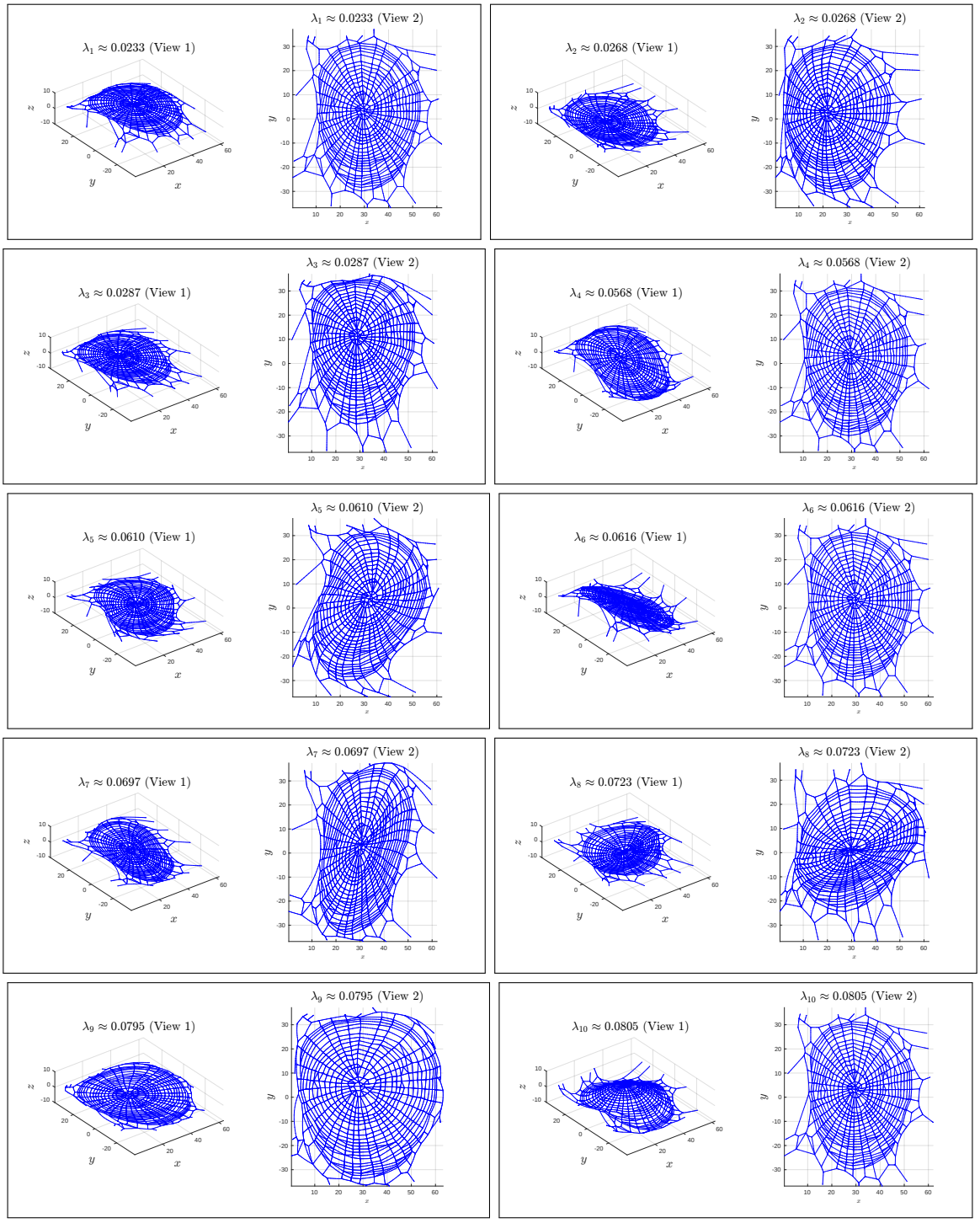

Figure 4.5: Eigenmodes for the real web shown in Figure 4.2.

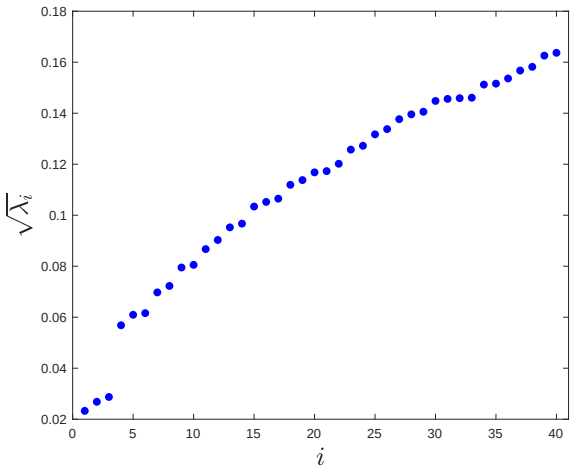

Figure 4.6: Eigenvalue distribution of first 40 eigenvalues for the orb web in Figure 4.2, using regular .

4.3 Non-uniform Dynamics

In an effort to provide biologically relevant results, we now account for the differences in the silks of the orb web shown in Figure 4.2. Several limiting factors arise when attempting to reconcile our model to the properties of different silks that biologists report in the field. As mentioned in Chapter 1, there are vast differences between the radial strands and catching spiral strands in an orb web. The translation of the reported parameters into our model proved more intricate than expected. The limitations and assumptions made when translating biological properties to the model are discussed below.

4.3.1 Biological and Model Limitations

The boundary and continuity conditions of the mechanical model do not require the knowledge of any physical parameters of string i other than its orientation in space, thus they remain the same as before. Equations (2.3) and (2.8), however, require knowledge of ρ^i, k^i,

and σ^i. Previously, we set each of these parameters to convenient uniform values, but now we look to reported material properties to add additional validity to the model.

Silk Density The model accounts for the linear density of each individual string within the network. Unfortunately, the density of spider silk it not reported accurately due to limitations in measuring mass of such a lightweight structure. Here we assume uniform density (kg/cm^3) of the radial and spiral strands throughout the orb web. For simplicity we assume the density is 1kg/cm^3; changes to this uniform density would scale the eigenvalues but not change the mode shapes. As the model requires linear density, we must then account for the cross sectional area, A, of each strand. Then linear density, $\rho = 1\text{kg/cm}^3 \cdot A$ cm^2, has units kg/cm. Possible methods to determine true density using our model are discussed in Chapter 5.

Cross Sectional Area Since a radial string is made of two parallel fibers, we assume the total cross sectional area to be twice the cross sectional area of one of these individual strands. We assume the strands are cylindrical, with circular cross sectional area. Let A_r represent the cross sectional area of a radial string. Using the values reported by [18], we have $A_r = 1.635^2\pi$ μm^2 or $A_r = 2.6732\pi \times 10^{-8}$ cm^2. (We do not model friction between these strands.) As mentioned in Chapter 1, determining the cross sectional area of catching spiral strands proves to be a more difficult task. The structure, comprising two thin strands, an aqueous sheath, and large glue droplets, begins to resemble a beaded string [2]. Our model considers each strand as a uniform thickness; to consider nonuniform cross sectional area would require a different approach, which is mentioned later as a possible extension. Modeling the catching spiral strands then leads us to the important decision of how to calculate the cross sectional area of each string. We will test two different methods of determining the area.

Internal Tension Equations (2.1) and (2.2) also account for an internal measure of tension σ^i. This is a constant that determines if the string is taut ($\sigma^i > 1$) or compressed ($\sigma^i < 1$). As we do not have values reported from the field pertaining to how stretched an individual strand is within a spider web, we are left to make assumptions about appropriate values. We assume all i strings are stretched with $\sigma^i = 2$. We will later show an example of what occurs when we drop this assumption, and allow different parameter values for radial and spiral strands.

Stiffness/Tension The parameter k^i correlates to the tension of an individual string. Biologists report Young's modulus, E, a measure of stiffness of an object, which is represented as the energy per cross-sectional area it requires to stretch a material [15]. The model gives the parameter k^i measured in Newtons. Thus to convert the Young's modulus to the stiffness k^i, we multiply by the cross-sectional area, A_s (for the catching spiral) or A_r (for the radial strands). We apply all appropriate conversions to ensure consistency between units within the model.

4.3.2 Structural Dynamics

As discussed in Chapter 1, the radial strands provide the main structural integrity of an orb web [3]. Figure 4.7 shows the radial structure of the orb web in Figure 4.2. With only the radial strings, the web now has 633 nodes and 678 strings. (Recall that we classify the frame threads that anchor the web as radial strings.) Here $k^i = EA_r = 8.7341$ kg·cm/s^2 and $\sigma^i = 2$. Assuming strand density 1 kg/cm^3, linear density

$$\rho^i = 1\text{kg/cm}^3 \cdot A_r\text{cm}^2 = 1.6796 \times 10^{-7}\text{kg/cm}.$$

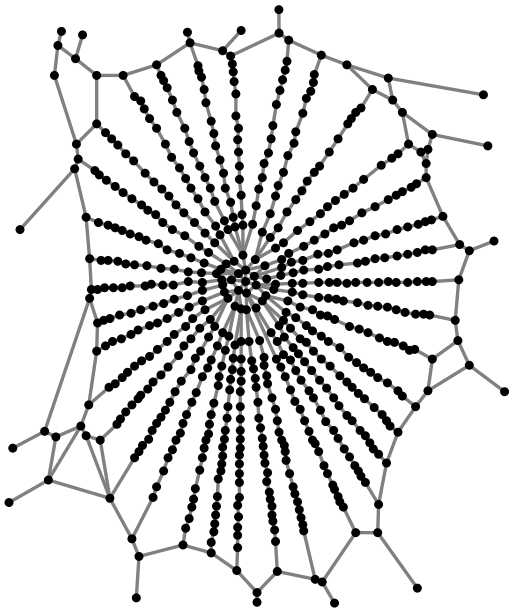

Figure 4.7: Orb web from Figure 4.2 with only the radial strands intact.

Then we solve the generalized eigenvalue problem of dimension 34578×34578 when $N = 16$. Figures 4.8 and 4.9 show the first 20 eigenmodes of the structural components of the web. Again, the first eigenmode exhibits drum-like movement in the z direction and shifting in the x-y plane for λ_2 and λ_3. Apart from these modes, the remaining eigenmodes shown have unique movements. Note that in several modes (λ_6, λ_8, λ_9, and λ_{10}) the lower strands stray from their original positions, while the the top strands show little to no movement.

4.4 Orb Web Dynamics

Returning to the original structure with radial strands and catching spiral, we implement several different sets of parameters to study the differences in dynamics.

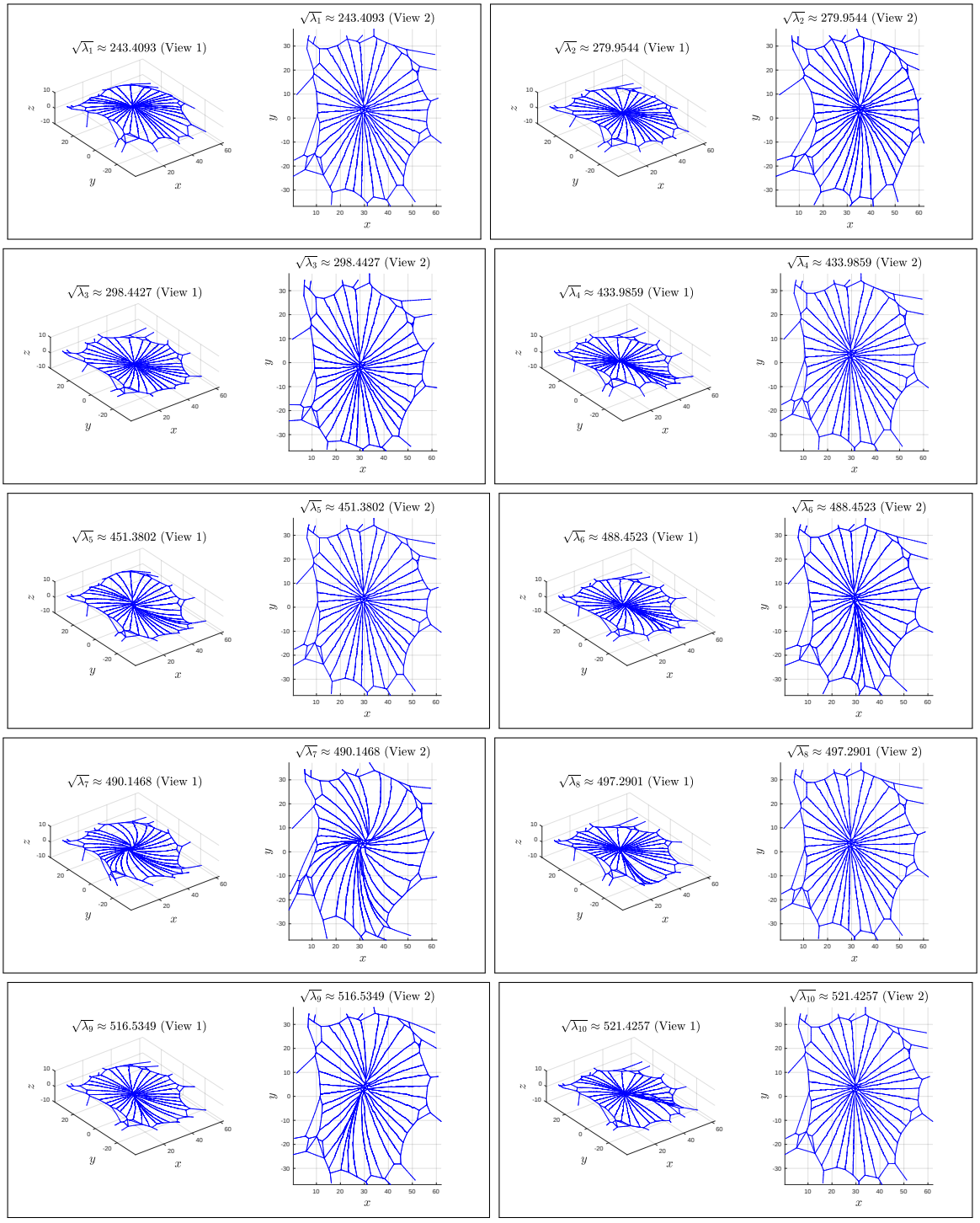

Figure 4.8: Eigenmodes corresponding to $\lambda_1, \ldots, \lambda_{10}$ for the orb web, using only radial edges as shown in Figure 4.7.

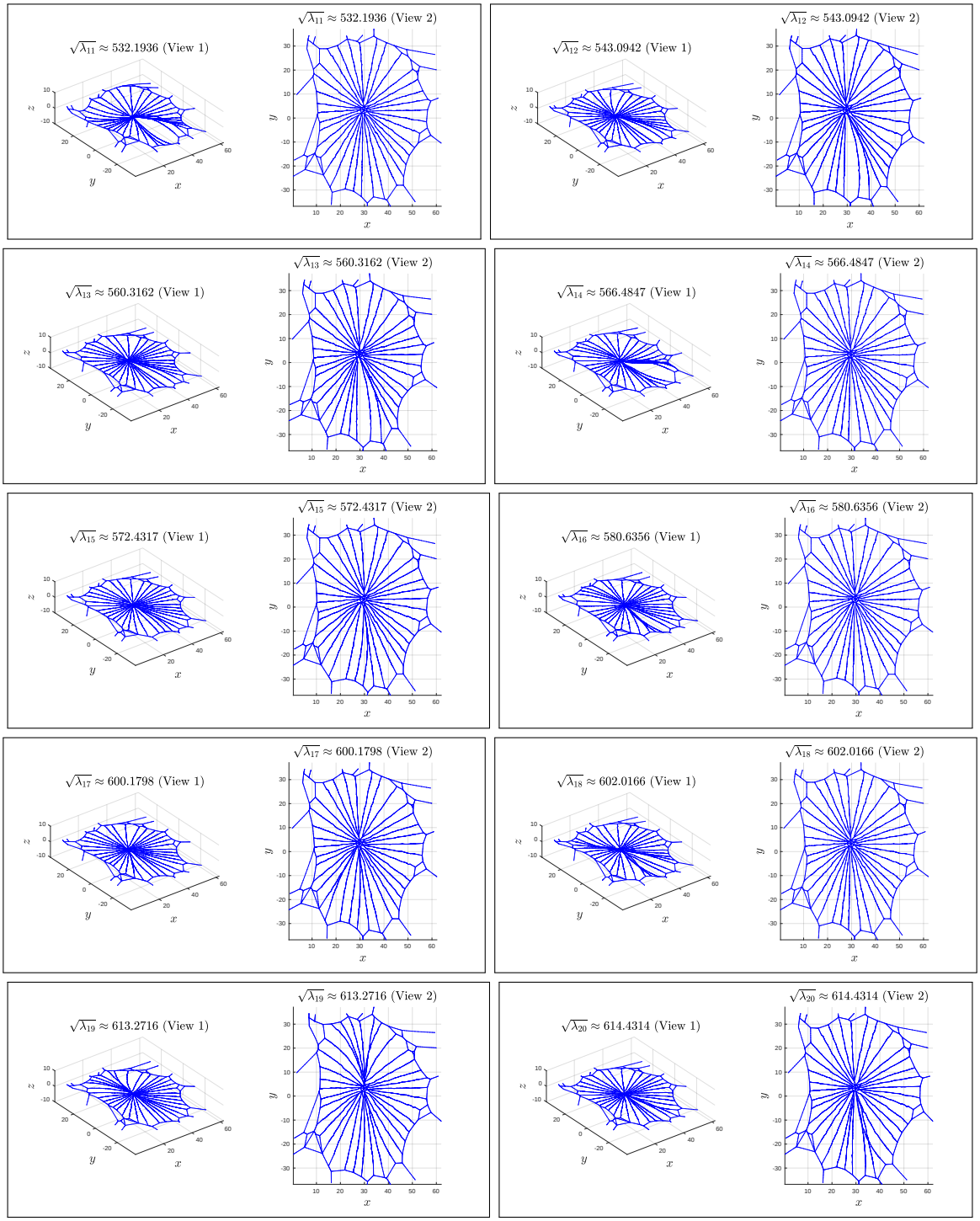

Figure 4.9: Eigenmodes $\lambda_{11}, \ldots, \lambda_{20}$ of the orb web, using only radial edges, as shown in Figure 4.7.

4.4.1 Example 1

Taking the orb web in full, we analyze the essential vibrations when considering an "average" cross-sectional area of the catching spiral strands. Liao et al. [11] conclude a "universal" formula for the volume of individual glue droplets on catching spiral threads. They accurately represent the shape of glue droplets as a parabola rotated around its axis. Using this observation, we estimate the average width of a droplet as

$$\left[\frac{2w}{\ell^2}\int_{-\ell/2}^{\ell/2}(\ell/2-x)(\ell/2+x)dx\right]\Big/\ell,$$

where ℓ is the length of the droplet along the strand and w is the widest point of the droplet. This leads us to an average radius of $r = w/3$. Opell [14] reports the average length and width of *Argiope trifasciata* droplets at 55% humidity as 54 μm and 40 μm respectively. Then using the fact that there are 160 droplets of length 54 μm per centimeter of catching spiral thread with average radius $r = w/3$ and the remaining length of each centimeter has two strands of radii 1.45 μm, we conclude the average cross-sectional area is $A_{avg} = 4.8435 \times 10^{-6}$ cm^2, using appropriate conversion factors to match units. This calculation gives

$$k^i = EA_{avg} = 0.3875\text{kg} \cdot \text{cm/s}^2.$$

Again we use $k^i = 8.7341$ kg·cm/s^2 for all radial strands and $\sigma^i = 2$ for all (radial and spiral) strands.

These parameter values lead to the eigenmodes shown in Figures 4.10 and 4.11. The first mode follows the same drum-like pattern we see in the other webs. Note how the dynamics of the orb web change from the uniform case (Figure 4.5). We see similar movements in the first three eigenmodes. The higher eigenvalues, however, begin to stray away from those of

the uniform web. The webs no longer have the symmetric movements observed previously. Note the squishing modes of λ_9 and λ_{10}; the bottom half of the web is squishing more than the top in both modes. In each mode, the catching spiral strings exhibit more movement than when assuming uniform dynamics (as seen in Section 4.2.1). This change is best seen in higher eigenmodes, such as for λ_{10} in Figure 4.10. This additional movement is expected since the spiral strands are more elastic than the radial ones.

Comparing the eigenmodes of the orb web with the spiral strings and without, we see a few variations in the eigenmodes. The first three appear almost identical, while the biggest difference appears to occur in the tenth eigemode. In the structural modes, Figure 4.7, the tenth mode oscillates up and down with no movement in the x-y plane. Conversely, λ_{10} in Figure 4.10 pinches toward the center.

4.4.2 Example 2

Rather than computing the average cross-sectional area, we could also assume the cross-sectional area is computed the same as for the radial webs, neglecting the glue droplets. Then we have the cross-sectional area $A_s = 2 \times (1.45 \times 10^{-4})^2\pi$ cm^2. Again $k^i = 0.3875$ kg·cm/s^2 for the spiral strands. We use $k^i = 8.7341$ kg·cm/s^2 for all radial strands and $\sigma^i = 2$ for all (radial and spiral) strands. Figures 4.12 and 4.13 give the dynamics of the system using these parameters. Previously, the dynamics of each web have followed a similar pattern, with small variations based on web shape, size, and parameters. These dynamics, however, exhibit drastic differences from the previous webs. Many of these modes exhibit movement only in a few strings, rather than as an entire web. Here, we highlight each string that exhibits significant movement within an eigenmode in blue. The remaining strings with little to no movement are depicted in gray. Note that the first ten eigenmodes have movement in several strings in the top right-hand corner of the web. Higher frequencies do

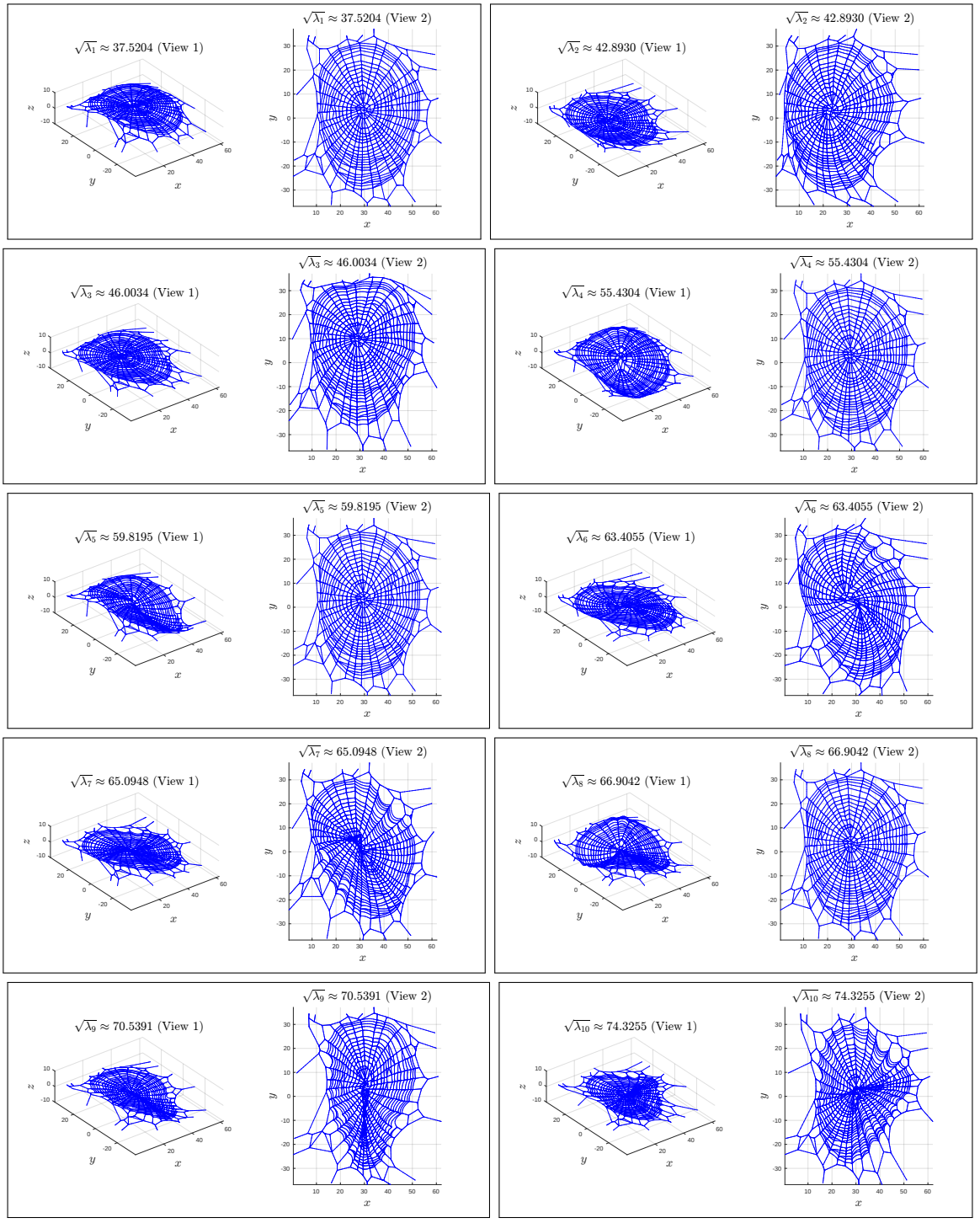

Figure 4.10: Eigenmodes $\lambda_1, \ldots, \lambda_{10}$ of the orb web in Example 1 (accounting for glue droplets on the spiral strands).

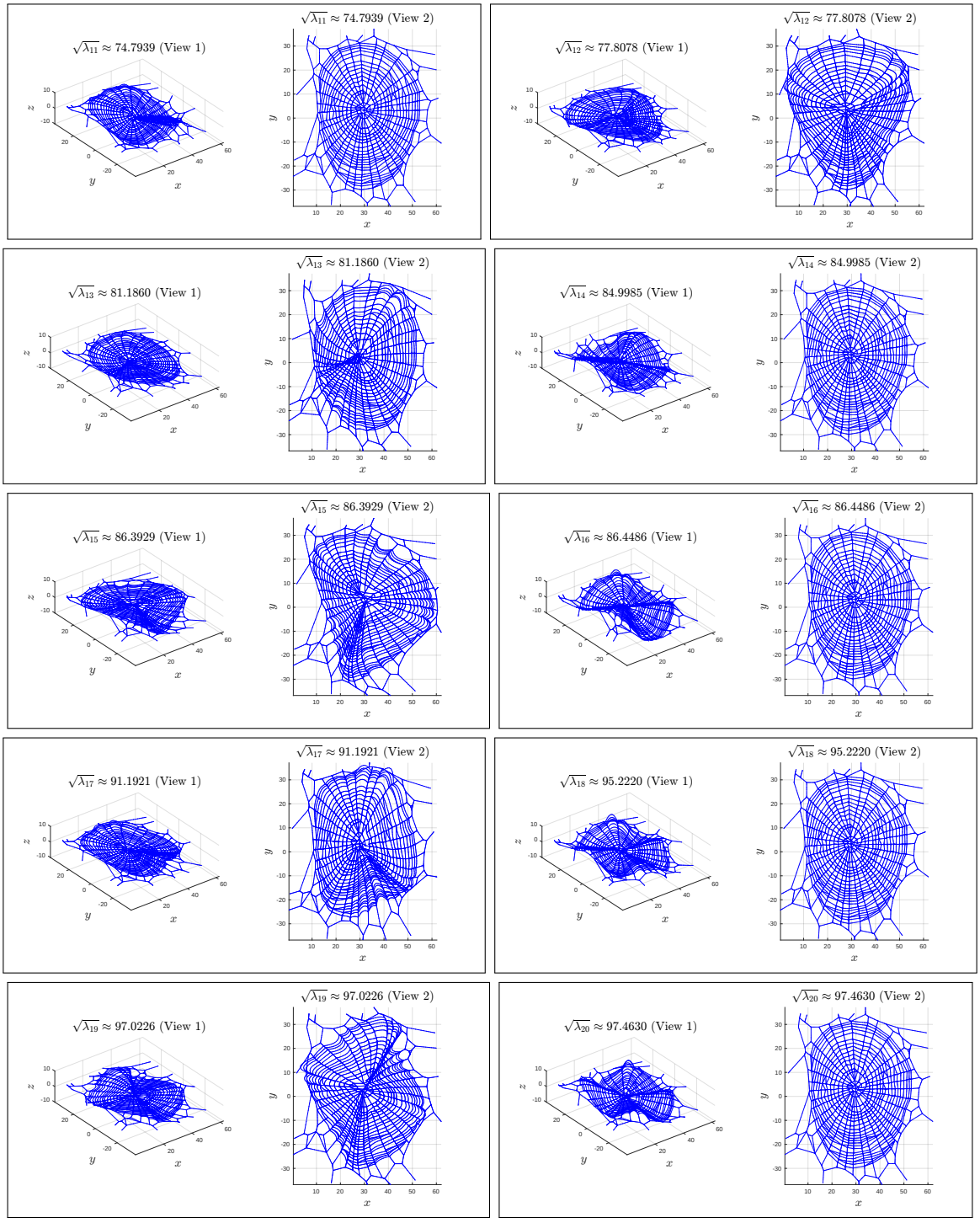

Figure 4.11: Eigenmodes $\lambda_{11}, \ldots, \lambda_{20}$ of the orb web in Example 1 (accounting for glue droplets on the spiral strands).

display global modes, such as those shown in Figure 4.14. However, even with these global modes, the dynamics of the system do not agree with our expectations for vibrations of a spider web. With each of the modes displayed for this example, the spiral strings are much thinner and more elastic than those of the radial strings. Thus the essential movements appear as if each spiral segment is considered as a vibrating string with rigid endpoints. We do not expect that this example is the best model of the vibrations of a biologically realistic spider web.

4.4.3 Example 3

In this example, we will use the same parameter values mentioned in Example 2 except for σ^i. In all previous runs, we assumed $\sigma^i = 2$ for all i. If we assume the spiral strands are "more stretched" than the radial and let $\sigma^i = 4$ for spiral strands i, and $\sigma^i = 2$ for all radial strands i, we see the dynamics in Figures 4.15 and 4.16. Here we see global modes for the first 6 eigenmodes. These modes have little to no movement of the structural components, but the spiral strands are shifting. The seventh eigenmode, however, exhibits similar movements seen for Example 2, with only the spiral strands in the top right-hand corner moving. At higher frequencies, global and localized modes are interspersed, as shown in Figure 4.16.

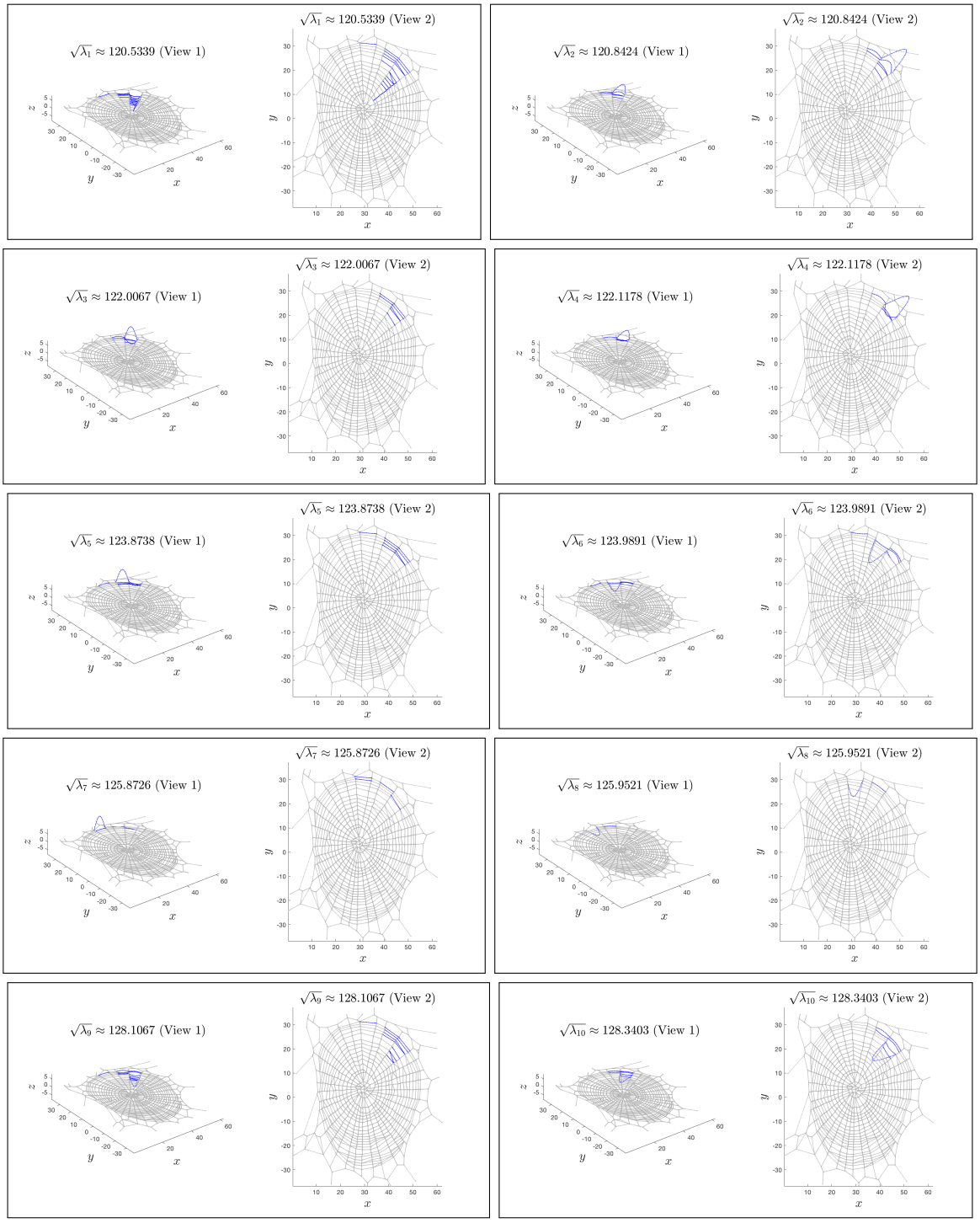

Figure 4.12: Eigenmodes $\lambda_1, \ldots, \lambda_{10}$ of the orb web in Example 2 (neglecting glue droplets).

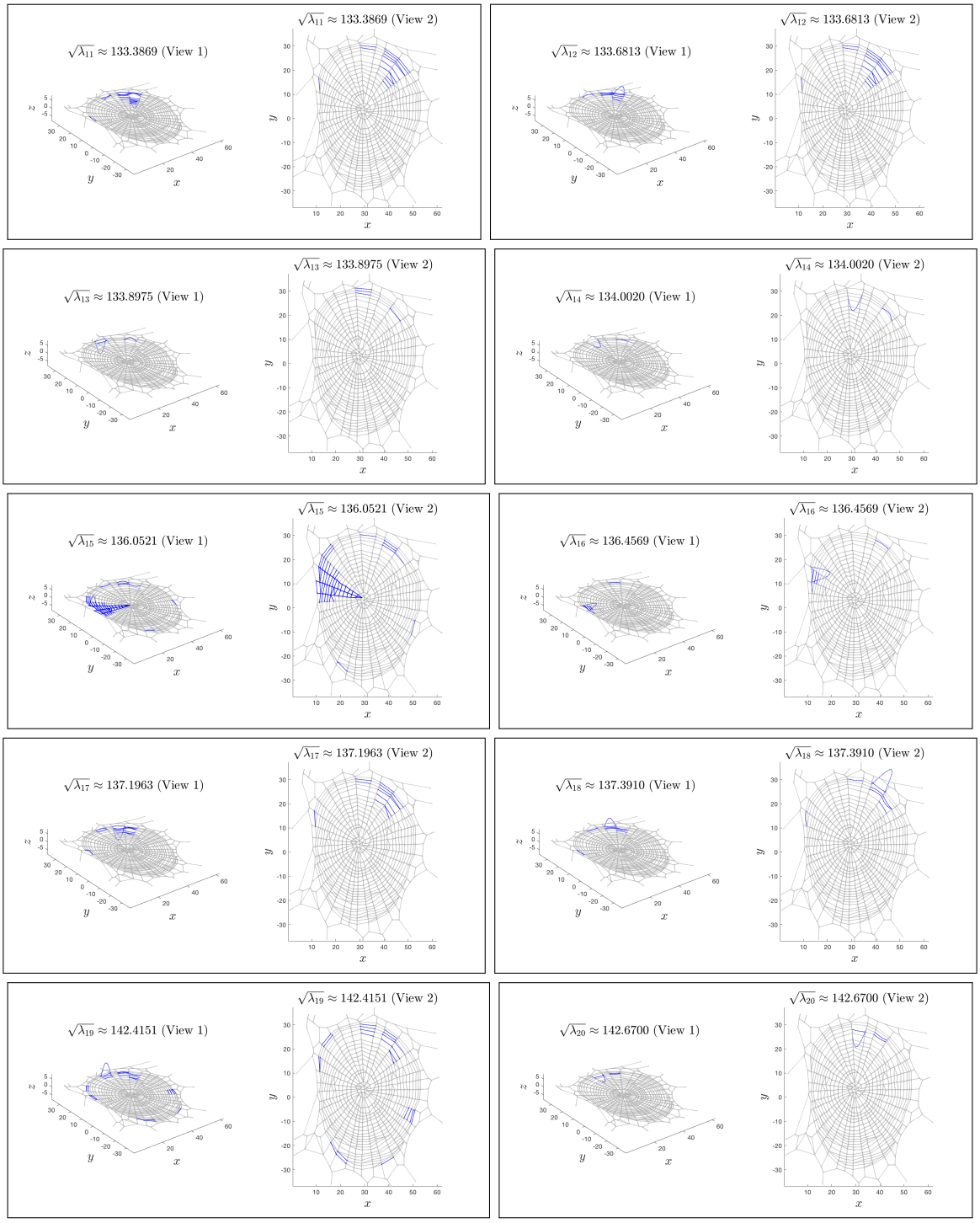

Figure 4.13: Eigenmodes $\lambda_{11}, \ldots, \lambda_{20}$ of the orb web in Example 2 (neglecting glue droplets).

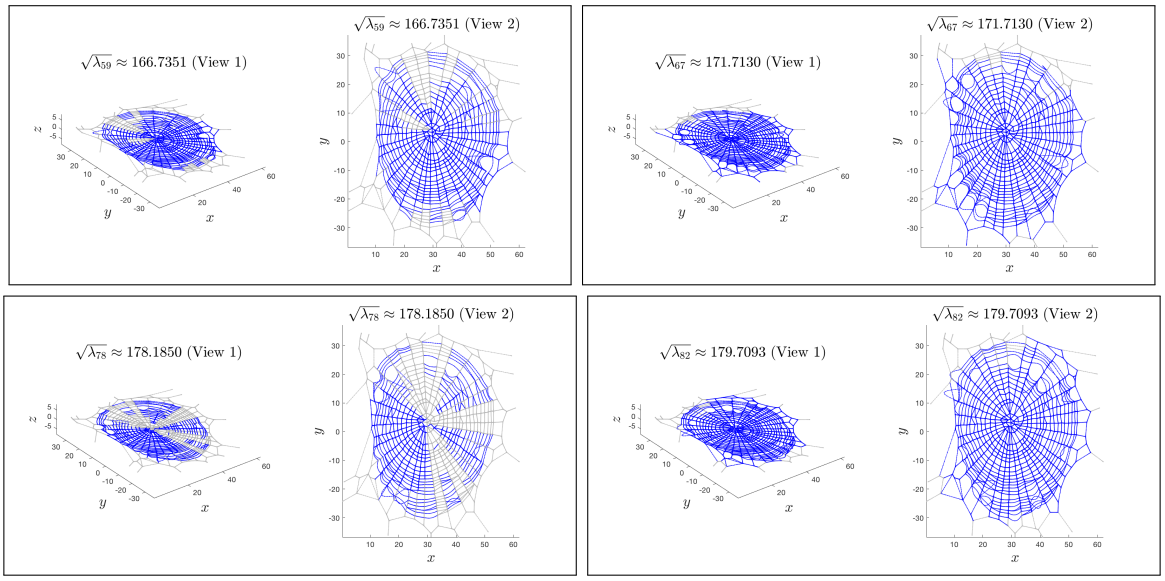

Figure 4.14: Higher eigenmodes that display global vibrations of the orb web in Example 2 (neglecting glue droplets).

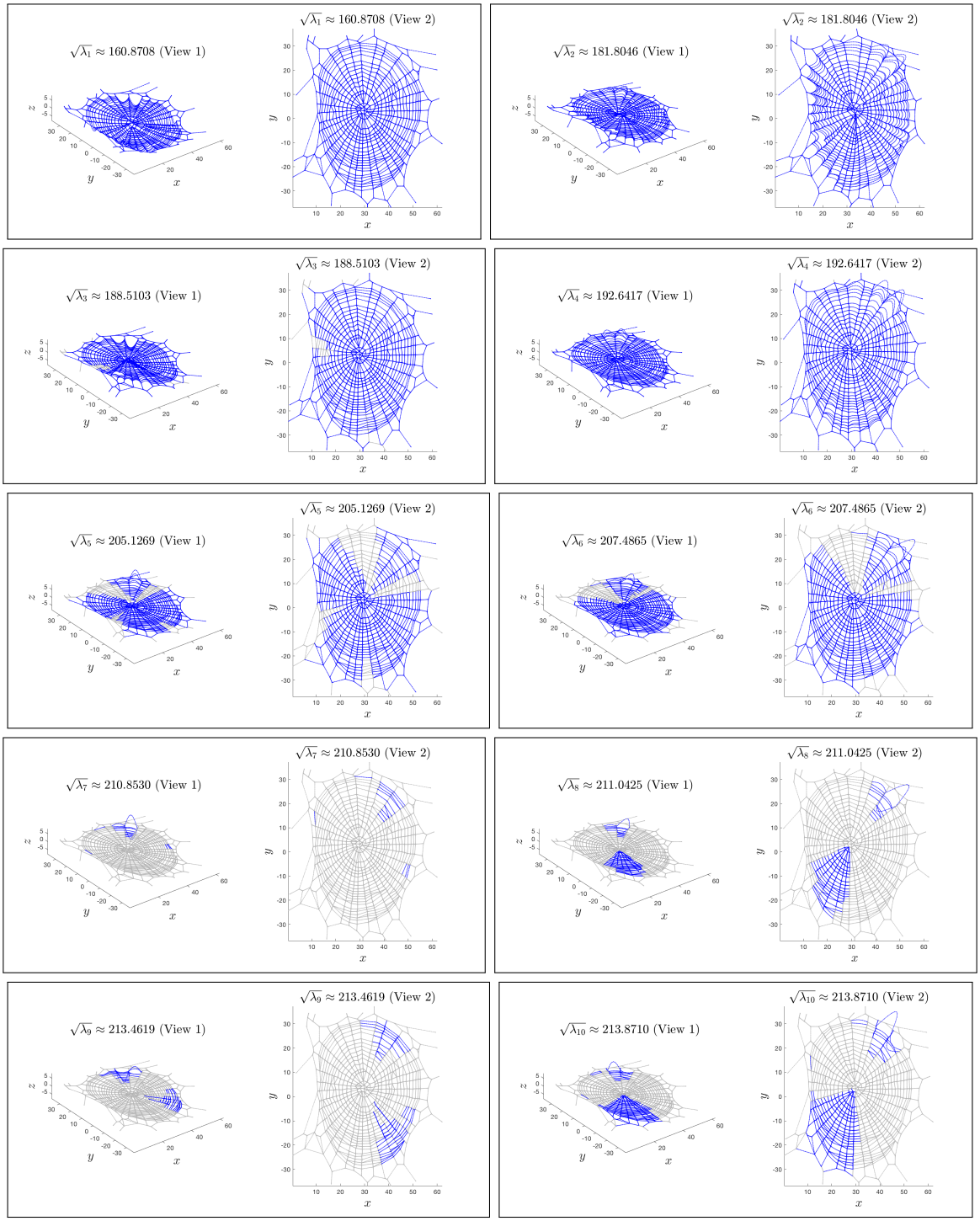

Figure 4.15: Eigenmodes $\lambda_1, \ldots, \lambda_{10}$ of the orb web in Example 3 (neglecting glue droplets, but nonuniform σ^i).

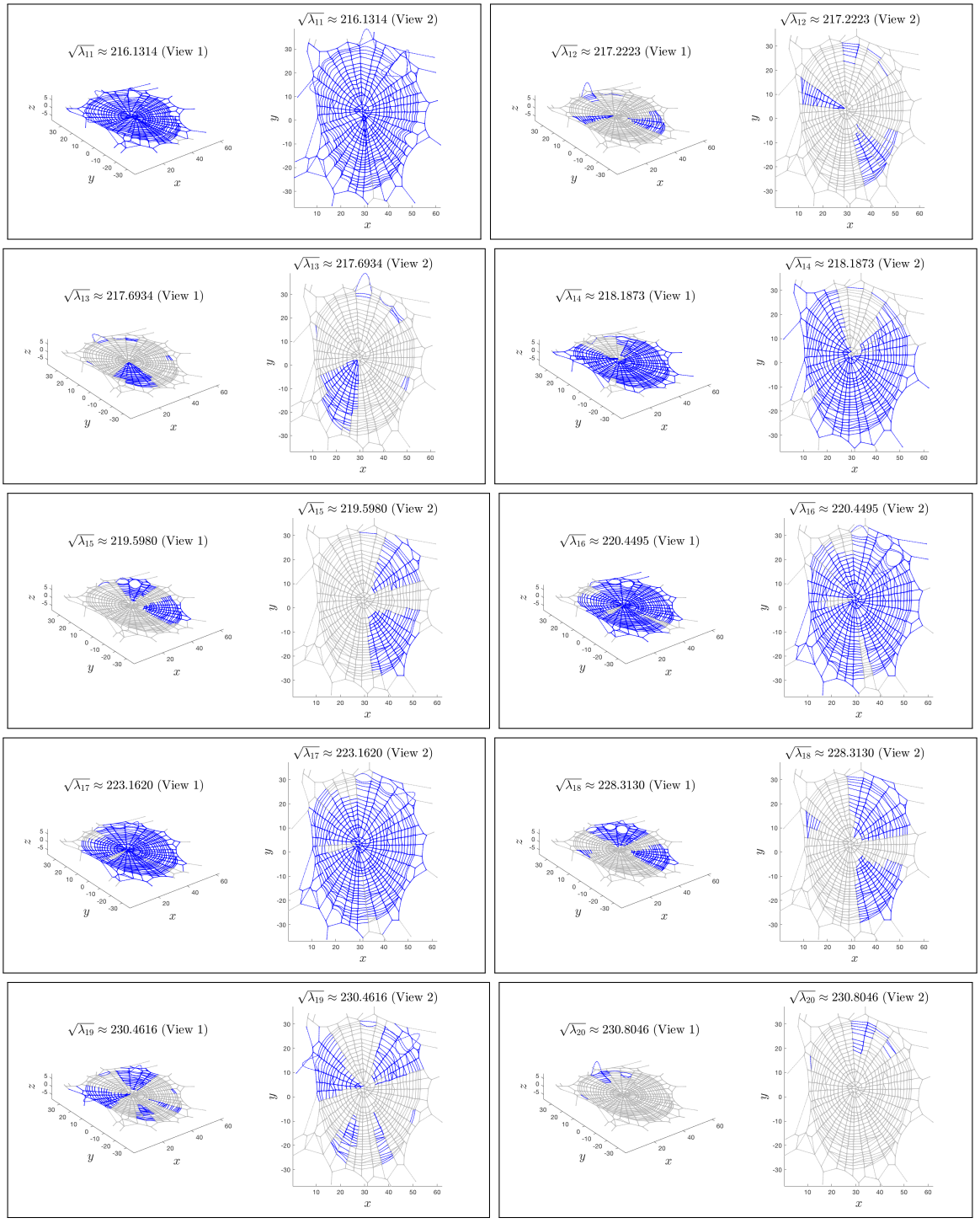

Figure 4.16: Eigenmodes $\lambda_{11}, \ldots, \lambda_{20}$ of the orb web in Example 3 (neglecting glue droplets, but nonuniform σ^i).

Chapter 5

Conclusions

The preceding chapters have illustrated how vibrations of biologically-realistic spider webs can be modeled via the wave equation on a multi-linked structure. This endeavor has revealed a number of areas that are ripe for additional investigation. Currently, biologists only report the diameters of the glue droplets and of the individual silk strands within the catching spiral. They do not, however, report the diameter of the aqueous sheath between droplets that encases the silk strands. Accounting for this added mass/dimension may also provide more interesting results. Additionally, the density of the strands shows itself as a scaling factor for the eigenvalues of the system. Thus, upon experimental testing of an actual spider web to determine its essential movements, we can calibrate the model of that exact web to those same movements. Assuming biologically accurate parameters for all values except for ρ^i within the spider web, the model could be combined with vibration experiments in a lab on actual webs to determine a single constant ρ for all the strands.

The transition to biologically realistic parameters illustrated uncertainties in the model. There are many questions to be answered in this area. One of the limitations of the model is also one of the biggest avenues for future work; the beaded string problem. Here we assume

each string to be a perfect cylinder, when in reality, none of the silk strands are. The radial strands are two smaller silk threads running parallel alongside each other, while the catching spiral strands have an even more complex structure. Our current model does not seek to model the glue droplets regularly spaced along the the catching spiral strings. Since these droplets are massive compared to the strings, they could be modeled as point-mass beads on a string; see, e.g., [2]. To add to the complexity, the diameters and characteristics of the radial and catching spiral strands vary between different species of orb weavers. Additionally, we arbitrarily chose values of σ for the stretched component of each string. While we attempted to logically determine the appropriate proportions and values for σ^i on each string, we have no biological evidence for the values displayed. To improve the model, we need to better understand the importance of σ for each strand and how it affects the dynamics.

The work done here has developed an efficient numerical discretization tool that allows for accurate determination of eigenvalues to high precision. This tool can enable significant research into web vibrations, e.g., by exploring web decorations. Many species of orb weavers, including *Agriope trifasciata*, add decorations to their webs. For this specific spider, these decorations often appear as thick zig-zag patterns occurring between two adjacent radial strands. The silk in such locations is distributed much more densely than in the rest of the web. The purpose of these decorations has been highly debated [5, 16]. Using the tool developed here, we could explore the effects decorations have on the vibrations of spider webs, and whether or not they have structural significance.

Bibliography

[1] S. J. Cox. Setting and solving the string net equations. Summer 2006. Unpublished notes.

[2] S. J. Cox, M. Embree, and J. M. Hokanson. One can hear the composition of a string: experiments with an inverse eigenvalue problem. *SIAM Review*, 54(1):157–178, 2012.

[3] R. Das, A. Kumar, A. Patel, S. Vijay, S. Saurabh, and N. Kumar. Biomechanical characterization of spider webs. *Journal of the Mechanical Behavior of Biomedical Materials*, 67:101–109, 2017.

[4] M. Embree. Eigenvalues of the tritare in two dimensions. Unpublished notes, 2018.

[5] R. Foelix. *Biology of Spiders. 3rd.* Oxford University Press, Oxford, 2011.

[6] S. Gaudet, C. Gauthier, S. Léger, and C. Walker. The vibrations of a real 3-string: the timbre of the tritare. *Journal of Sound and Vibration*, 281(1-2):219–234, 2005.

[7] M. S. Gockenbach. *Partial Differential Equations: Analytical and Numerical Methods.* SIAM, Philidelphia, 2005.

[8] J. E. Lagnese, G. Leugering, and E. G. Schmidt. *Modeling, Analysis and Control of Dynamic Elastic Multi-link Structures.* Springer, New York, 2012.

[9] M. Landolfa and F. Barth. Vibrations in the orb web of the spider nephila clavipes: cues for discrimination and orientation. *Journal of Comparative Physiology A*, 179(4):493–508, 1996.

[10] R. B. Lehoucq, D. C. Sorensen, and C. Yang. *ARPACK Users' Guide*. SIAM, Philadelphia, 1998.

[11] C.-P. Liao, S. J. Blamires, M. L. Hendricks, and B. D. Opell. A re-evaluation of the formula to estimate the volume of orb web glue droplets. *The Journal of Arachnology*, 43(1):97–100, 2015.

[12] W. Masters. Vibrations in the orbwebs of nuctenea sclopetaria (araneidae) I. Transmission through the web. *Behavioral Ecology and Sociobiology*, 15(3):207–215, 1984.

[13] W. Masters. Vibrations in the orbwebs of nuctenea sclopetaria (araneidae) II. Prey and wind signals and the spider's threshold. *Behavioral Ecology and Sociobiology*, 15:217–223, 1984.

[14] B. D. Opell. Agriope trifasciata properties of catching spiral droplets. Unpublished observations, 2016.

[15] B. D. Opell, D. Jain, A. Dhinojwala, and T. A. Blackledge. Tuning orb spider glycoprotein glue performance to habitat humidity. *Journal of Experimental Biology*, 221(6):jeb161539, 2018.

[16] F. Punzo. *Spiders: Biology, Ecology, Natural History, and Behavior*. Brill Academic, Leiden, 2007.

[17] E. G. Schmidt. On the modelling and exact controllability of networks of vibrating strings. *SIAM Journal on Control and Optimization*, 30(1):229–245, 1992.

[18] A. Sensenig, I. Agnarsson, and T. Blackledge. Behavioural and biomaterial coevolution in spider orb webs. *Journal of Evolutionary Biology*, 23(9):1839–1856, 2010.

[19] S. D. Stellwagen. *Structure and Function of the Viscous Capture Spiral and its Relationship to the Architecture of Spider Orb Webs*. PhD thesis, Virginia Tech, 2015.

[20] L. N. Trefethen. *Spectral Methods in MATLAB*. SIAM, Philadelphia, 2000.